Original Article

Generation of nanopore structures in yttria-stabilized zirconia by femtosecond pulsed laser irradiation

Yuka Yamamuro [a], Tomotaka Shimoyama [b], Jiwang Yan [a,*]

[a] School of Integrated Design Engineering, Graduate School of Science and Technology, Keio University, Hiyoshi 3-14-1, Kohoku-ku, Yokohama, 223-8522, Japan
[b] Inorganic Materials Research Laboratory, TOSOH Corporation, Hayakawa 2743-1, Ayase, 252-1123, Japan

ARTICLE INFO

ABSTRACT

Femtosecond pulsed laser irradiation of yttria-stabilized zirconia (YSZ) was performed to investigate the feasibility and fundamental characteristics of nanopore structure fabrication. Numerous nanopores were successfully generated on the YSZ surface with only a single laser pulse shot by controlling laser power near the ablation threshold. The nanopore generation mechanism involves light focusing by the convex shape of a crystal grain and ablation inside the grain. By increasing laser power, the number of nanopores increased. Cross-sectional observation revealed that the depth of nanopores was about 500 nm, and nanopores were generated inside the YSZ grains of the top layer while keeping the grains' shapes unchanged. It was found that higher scanning speed and a small number of scans enabled nanopores fabrication without changing the original surface shape, avoiding the removal of the surface layer. Laser-irradiated surfaces of YSZ were characterized by Raman spectroscopy, and it was found that there was no significant phase change in the specimen after nanopore generation compared with the original YSZ surface, confirming that there was no thermal damage to the bulk material. The surface with nanopores showed an enhancement in surface hydrophilicity. These findings demonstrated the possibility of selectively generating nanopores in the top surface of YSZ for use in functional surfaces without serious thermal damage to the workpiece. It is expected that the nanopore generation will lead to new applications of YSZ.

© 2023 The Author(s). Published by Elsevier B.V. This is an open access article under the CC BY license (http://creativecommons.org/licenses/by/4.0/).

1. Introduction

Zirconia (ZrO_2) is a ceramic material with excellent heat resistance, hardness, and chemical stability. It is an ionic crystal composed of Zr^{4+} and O^{2-}. Zirconia usually has a monoclinic crystal structure at room temperature. With an increase in temperature, the monoclinic phase undergoes phase transformation resulting in the formation of tetragonal and cubic phases. However, this phase transformation is accompanied by a volume change, e.g., a 4% volume shrinkage in the monoclinic-tetragonal phase transformation. This

causes material fracture due to temperature change. To solve this problem, small amounts of metal oxides such as Y_2O_3, MgO, CaO, and CeO_2 are added as dopants to zirconia to stabilize the tetragonal and cubic phases at room temperature, which are generally only stable at high temperatures. Zirconia produced in this way is generally called stabilized zirconia. It is possible to suppress material fracture caused by temperature change. In particular, the zirconia with Y_2O_3 as a dopant is called yttria-stabilized zirconia (YSZ), and is an important fine ceramic material that has increasing demand in various fields. Polycrystalline tetragonal YSZ has high strength and high fracture toughness at room temperature [1]. These material characteristics are due to the effect of the stress-induced phase transformation mechanism, whereby the tetragonal phase undergoes a local phase transformation to a monoclinic phase due to stress loading when small cracks occur, resulting in volume expansion, and the compressive stress on the crack tip inhibits its propagation [1]. In addition, YSZ has low thermal conductivity, chemical stability, and unique aesthetic effects. Due to its superior properties, YSZ has been used as a biomaterial component [2], and in recent years it has been used in many other applications such as dental implants, optical fiber connectors, and solid oxide fuel cells.

For biomaterial application, it is essential to enrich the surface functionality to obtain better biocompatibility. For example, dental implants are required to promote osseointegration, i.e., the affinity between the implant material and bone. By promoting osseointegration, implants can be fixed in the bone quickly and strongly. Conventionally, titanium has been used as an implant material and subjected to various chemical and physical surface treatments to improve its affinity with body tissues. To achieve surface affinity, sandblasting, chemical treatment, and plasma spraying have been used to roughen the surface and make it porous with micro and nanoscale pores. Hou et al. [3] revealed that dental implants with micro/nanoporous surfaces had good biocompatibility. Furthermore, Salou et al. [4] reported that nanostructured surfaces improve osseointegration as much as or better than microstructures. Surface functionalization of YSZ in various other fields has also been actively studied in recent decades. Surfaces with micro and nanoscale structures can change many surface functionalities such as wettability [5], anti-fouling [6], and frictional properties [7]. In particular, porous surface structures are expected to enhance wettability by increasing the surface area, improve the adhesiveness by the anchoring effect, and function as a carrier for different materials such as drug delivery systems [8]. Therefore, porous surface generating technology is crucial for enhancing surface functionality and exploring new applications of zirconia products. In addition, it is desirable to create pores only in the material surface layer since a fully porous bulk material has a low material strength.

However, it is still difficult to create the desired porous structures on the YSZ surface due to its excellent mechanical material properties. Machining of YSZ by various conventional mechanical methods such as cutting [9], grinding [10], and polishing [11] have been studied, but YSZ is difficult to be machined due to its high hardness. Moreover, these methods are only useful for machining flat or curved surfaces, while not suitable for the fabrication of micro and nanoscale pores.

In addition, sandblasting, a conventional rough surface machining method for implants, might lead to phase transformation of YSZ due to the extreme mechanical reaction on the surface. Scott [12] reported that YSZ mainly consists of tetragonal phases under atmospheric temperature and pressure conditions. However, due to the high stress and thermal conditions leading to the tetragonal phase partially changing into the monoclinic phase during certain machining processes, decreases the material strength [13]. Kosmač et al. [14] reported that sandblasting causes a tetragonal-to-monoclinic phase transformation, and a high amount of monoclinic phase that is created by stress loading during processing was found on the sandblasted surface. Grigore et al. [15] showed that the monoclinic phase was distributed up to a few micrometer depths under the surface. Other mechanical machining methods also cause such phase transformation to YSZ. In addition, localized and selective processing by chemical treatment is difficult, and the chemical stability of YSZ makes it difficult to fabricate surface structures by chemical etching [16]. Therefore, a new method is needed to selectively create nanoscale porous structures on the surface without extra machining damage to the material.

In this study, we propose a novel method for generating surface nanopores in YSZ by ultrashort pulsed laser irradiation. Compared to conventional mechanical and chemical processing methods, laser processing has many advantages. For instance, it is a non-contact process that does not require a machining tool, and its machining ability is independent of material hardness. Moreover, laser processing has a high flexibility in the machining area through the control of galvanometer scanning mirrors. Thus, selective surface fabrication can be performed over a large area in a short time. Furthermore, chemicals and coolants/lubricants generally used in conventional processes are not required for laser processing, thus reducing the impact on the environment. In addition, ultrashort pulsed laser ablation is known as one of the effective methods for minimizing thermal damage, which easily leads to micro and nanoscale structures. Long-pulse laser irradiation of YSZ normally induces thermal damage as the rise in temperature results in laser-induced tetragonal-to-monoclinic phase transformation. However, areas of YSZ that were irradiated by a femtosecond pulsed laser showed a lower percentage of the monoclinic phase [17]. This is because the pulse width of the femtosecond pulsed laser irradiation is much shorter as compared to the time taken for the heat transfer to occur. Delgado-Ruíz et al. [18] revealed that laser microstructuring by femtosecond pulsed laser ablation could remove most of the monoclinic phase that originally existed in the implants and did not induce a further increase in the monoclinic phase in the material surrounding the irradiated area. In addition, our previous study showed that the monoclinic ratio decreased by less than 1% by changing laser parameters [19]. When a laser other than a femtosecond laser is used, a significant increase in the monoclinic phase was observed by the picosecond pulsed laser process [20], and a molten layer with thermally induced cracks [21] and a high percentage (~10%) of monoclinic phase in the machined area [22] were observed by the nanosecond pulsed laser process. Hence, femtosecond pulsed laser irradiation is an effective method for YSZ to suppress phase transformation.

In laser processing, many kinds of micro and nanostructures can be fabricated by controlling laser parameters. Microgrooves are generated with high laser power, and nanoscale structures known as laser-induced periodic surface structures (LIPSS) with low energy near the ablation threshold. By decreasing laser power to a suitable level, it might be possible that only a small amount of material is removed from the surface, which enables fabricating a large area of nanopores on the surface layer of the material and creating porous structures. In this way, localized pore formation can be achieved without causing damage to the bulk layer, which is the most prevalent cause of material strength and life degradation of ceramics material. However, up to date, nanopores generation on YSZ by femtosecond pulsed laser irradiation has not been reported and the possibility and the effect of laser parameters on pores generation have also not been clarified.

Thus, in this study, femtosecond pulsed laser irradiation on YSZ was attempted to investigate the possibility and explain the fundamental characteristics of nanopore formation through a novel mechanism of light focusing by the convex shape of a crystal grain and ablation inside the grain, which has never been reported before. The effects of laser parameters on the irradiated surface morphology were clarified. Furthermore, the laser-induced structural change and surface chemistry of YSZ were evaluated. The objective of this work is to create nanopores that can provide a new approach to enrich the surface functionality of YSZ not only for dental implants but also for various other fields in the industry to enhance the surface functionality such as wettability, biocompatibility, and nanomedicine delivery.

2.   Experiments

The laser used in this study was an Yb: KGW laser PHAROS-08-600-PP, made by Light Conversion, UAB, Lithuania. The laser wavelength was 1028 nm and the pulse width was 256 fs at a repetition frequency of 100 kHz. The laser spot diameter was 20 μm at the focal point, and the focal length was approximately 70 mm. The laser beam had a Gaussian energy distribution. Fig. 1 shows the schematic of the experimental setup. A galvanometer scanner system was used to control the X- and Y-axis scanning of the laser beam, and laser motion programs were created with the WinLase Professional software. The workpiece was placed on the Z-axis stage, and an fθ lens was used to focus the laser beam onto the workpiece surface. The laser power was precisely controlled by the attenuator. The laser beam was scanned in a line for various irradiation parameters summarized in Table 1. The pulse width was set to the minimum value (256 fs) that can be produced by the laser system to minimize the thermal effect. Localized processing is necessary for pore formation, which is highly dependent on laser power. Therefore, the laser power was varied in a wide range so as to include the ablation threshold of zirconia, and the processed surface was investigated in detail by irradiating in 50 mW increments. The ablation threshold was determined based on our previous studies. When scanning the laser beam, the interval distance between irradiated pulses onto the workpiece increases as the scanning speed increases. In this study, the scanning speed
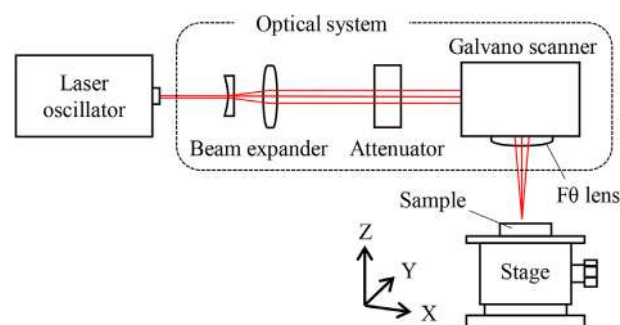

Fig. 1 — Experimental setup of laser optical system.

conditions were set so that the overlap rate was 0—100% to verify the difference in processing phenomena due to the overlap of pulses. The upper limit was determined to be 1000 mm/s, because above this speed the pulse overlap rate becomes insignificant (~0%), i.e., only the spacing between pulses is widened. The pulse frequency and scanning speed affect the pulse overlap rate. However, since the total output power of the laser is limited, increasing the frequency will decrease the laser energy per pulse. Hence, the frequency was fixed at 100 kHz, and the overlap rate was controlled by changing the scanning speed. In order to investigate the effect of repetitions, the laser was scanned multiple times and the maximum number of scans was set to 10 times, as above this, the zirconia surface with pores was completely removed.

As a workpiece, fully sintered YSZ polycrystalline containing 3 mol% Y_2O_3 for stabilization made by Tosoh Corp., Japan, was used. The sample was a rectangular plate with dimensions of 20 mm × 20 mm × 3 mm. The sample surface was sintered at 1500 °C and thermally etched at 1350 °C without polishing. The average grain size was 600 nm, and surface roughness was 309 ± 18 nm Ra.

After the irradiating laser, a scanning electron microscope (SEM), Inspect F50 produced by FEI Co., USA, was used to observe the surface morphologies of the samples. To measure the cross-sectional profiles of the irradiated surface, a laser microscope, OLS4100, made by Olympus Corp., Japan, was used. To investigate the cross-sections of pores, the sample was cut by an ultraprecision lathe Nanoform X, made by AMETEK Precitech Inc., USA. Fig. 2 shows the sample preparation method by cutting. An FE-SEM ZEISS GeminiSEM 500, made by Carl Zeiss AG, Germany, equipped with an EBSD

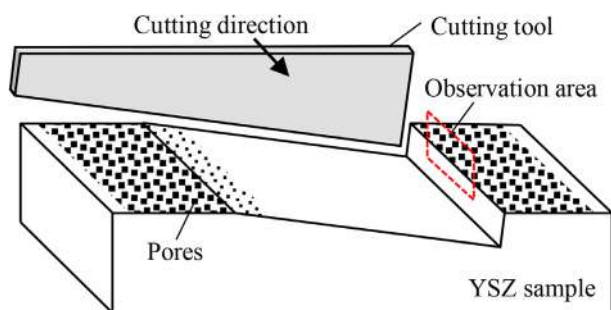| Table 1 — Experimental conditions.	
Laser medium	Yb: KGW
Wavelength [nm]	1028
Spot size: d [μm]	20
Pulse width [fs]	256
Repetition frequency: f [kHz]	100
Scanning speed: v [mm/s]	1.0–1000
Laser power: E [mW]	150–900
Laser fluence: F [J/cm^2]	0.48–2.86
Number of scans: N	1–10
Atmosphere	Air

Fig. 2 − Sample preparation method by cutting.

detector, made by EDAX Inc., USA, was used to identify the grain boundaries in a cross-section. The profile of the original surface structures was measured by an atomic force microscope (AFM), SPM-3, made by Hitachi High-Tech Corp., Japan. For quantitative evaluation of the pores, image analysis of the irradiated area was conducted with ImageJ software. The contours of the surface aperture of the pore were extracted from the SEM images by setting the threshold value according to the brightness to binarize the image, and then the number and size of pores were calculated. The pore ratio was calculated as the area fraction of pores per laser irradiated area (10 μm × 10 μm) and the average data of six images was used.

Moreover, a laser micro-Raman spectrometer, InVia Raman Microscope, made by Renishaw plc., UK, was used to evaluate the material phase structure. The laser wavelength of the Raman spectrometer was 532 nm, and the beam diameter was 1 μm. Chemical changes in the irradiated surface were evaluated by an X-ray photoelectron spectroscopy (XPS), JPS-9010TR, made by JEOL Ltd., Japan, and a glow discharge optical emission spectroscopy (GDOES), GD-Profiler2, made by HORIBA Ltd., Japan. Changes in surface wettability were evaluated by measuring the contact angle of the surface by a contact angle meter, Simage Entry 5, made by Excimer Inc., Japan. Contact angle measurements were made by a static sessile drop method, and 5.0 μL of purified water was used for a droplet.

3. Results and discussion

3.1. Nanopore formation phenomena

3.1.1. Effect of laser power
Line irradiation was carried out to investigate the effect of the laser power. The laser beam was scanned a single time at a scanning speed of 1000 mm/s with different laser power near the ablation threshold without causing the ablation of the top layer. Fig. 3 shows the SEM images of the irradiated surface at each laser power. When the laser power was lower than 400 mW, no pores were formed and no change in the YSZ surface occurred before and after the laser irradiation. At 400 mW, few pores sparsely formed on the zirconia grains on the surface. These pores were formed only in the center area

of the laser pulse. At 500 mW, the number of pores increased and formed uniformly within a circular region corresponding to the pulse shape. The diameter of the pores became larger in the center area of the pulse, and smaller pores were observed at the edge of the pulse. At 600 mW, the pores formed on neighboring grains combined and changed into larger elongated pores. These merged pores primarily formed in the center of the pulse, while individual nanopores still formed on zirconia grains at the outer edge of the pulse. This happens because of the Gaussian energy distribution of the laser beam. As the energy intensity is higher in the center of the beam, more energy absorption occurs in the YSZ grains in this area, resulting in formation of large pores. In addition, when the pore diameter reaches the size of a YSZ grain by increasing the laser power, the neighboring pores bond with each other to form larger pores. At 900 mW, the entire laser scanned area was ablated and a porous surface was formed. YSZ grain boundaries could not be observed in the irradiated area. According to these results, it was found that the nanopores formed in the grains at 400−600 mW, and the laser power was an important parameter to generate pores without removal of the top layer.

For further investigation of generated pores, detailed observation was performed. Fig. 4 shows magnified SEM images of the nanopores irradiated at a laser power of 500 mW. Nanopores were uniformly generated on each grain (Fig. 4(a)). The mouth of the pore had a smooth edge, and no cracks were observed (Fig. 4(b)). The wall surface inside the pore was very smooth and there was no debris adhesion (Fig. 4(c)). The bottom of the pore could not be observed from the SEM image. It was found that the nanopores were not shallow but were deep cavities inside the grains.

In order to investigate the internal structure of the nanopores in detail, cross-sectional observation was performed. Fig. 5 shows the SEM images of the cross-section of nanopores irradiated at 500 mW. The nanopores were formed only in the top layer of the material, as shown in Fig. 5(a). The pores were long and narrow, and the diameter of the pores inside the materials was larger than the diameter exposed on the surface of the grains. The depth of the pores was about 500 nm. This corresponds to the diameter of a single zirconia grain, confirming that the nanopores are formed in individual zirconia grains. In addition, as shown in Fig. 5(b), many cross-sections of pores were observed under the surface. Pores were formed at a depth of less than 1 μm from the surface. In particular, the pore, indicated by the arrows in the center of the image, formed vertically and elongated against the surface inside the zirconia, but the pore did not reach the surface and became a cavity within the grain. To identify the grain boundaries in the cross-section, EBSD analysis was performed. The inverse pole figure (IPF) map of the cross-section is shown in Fig. 5(c). The grain boundaries were clarified, and pores were formed on the top surface grain layer. Such nanopore structures have been difficult to be obtained by conventional mechanical or laser drilling methods.

3.1.2. Effect of scanning speed
The effect of laser scanning speed was investigated. Line irradiation was performed at a laser power of 400 and 600 mW, upper and lower limits of the power at which nanopores can
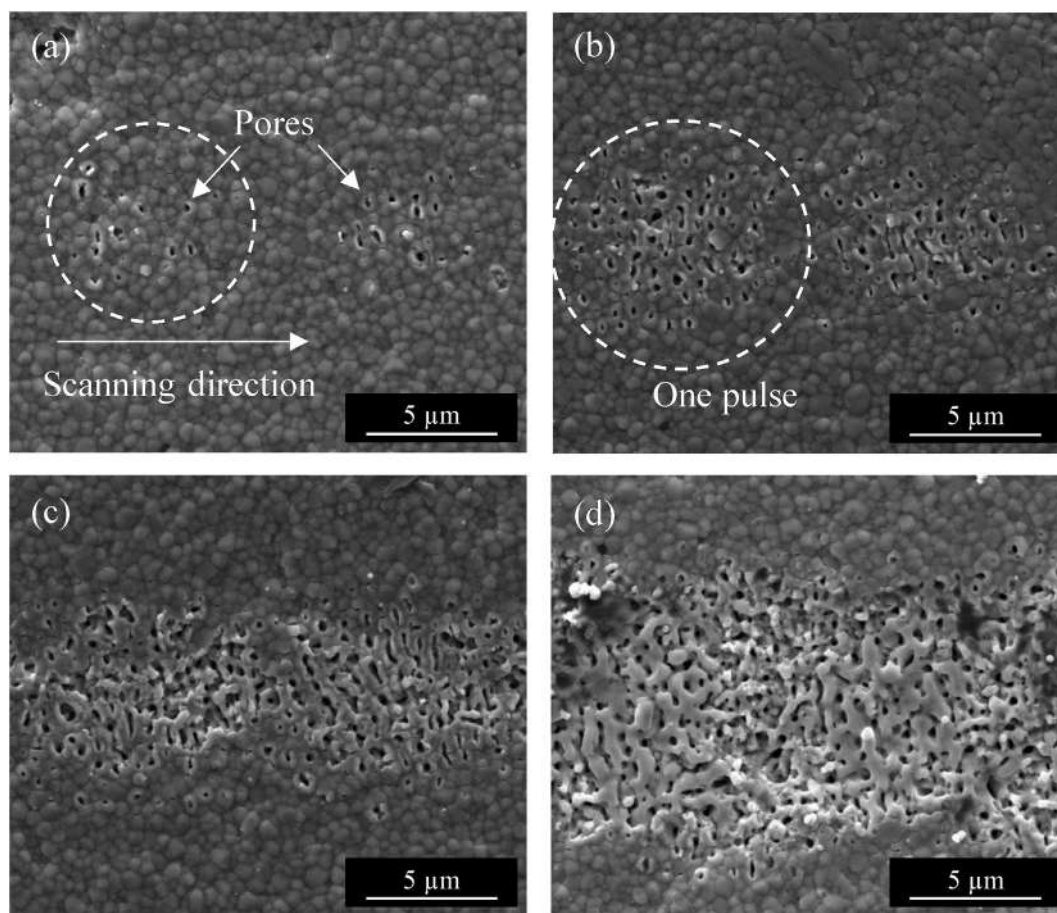
Fig. 3 – SEM images of irradiated surface under different laser power: (a) 400 mW, (b) 500 mW, (c) 600 mW and (d) 900 mW.

form, and a number of scans of $N = 1$ with different scanning speeds. Fig. 6 presents the SEM images of the irradiated surface at each scanning speed. When irradiated at 400 mW, nanopores formed in the grain on the surface at 400 mm/s. However, when the scanning speed decreased to 300 mm/s, some of the grains on the surface were completely removed. At a scanning speed of 200 mm/s, a microgroove formed on the entire irradiated surface. Similarly, at a laser power of 600 mW, the surface layer with nanopores generated on the YSZ grains was completely removed at a scanning speed of less than 700 mm/s. It was found that, at any laser power, decreasing the scanning speed resulted in ablation of the entire irradiated area. It can be attributed to the increase in the overlap rate of the laser pulses due to the decrease in scanning speed. As described in Fig. 3, pores formed only in the center region of the laser pulse due to the energy distribution of the laser beam, and the diameter of the circular processed area where the pores can form changed with the laser power. The diameter of the processed area when irradiated at 400 mW and 600 mW was about 5 μm and 10 μm, respectively. Based on these effective sizes of the laser spots for nanopore formation, the overlap rate was calculated. Fig. 7 shows the relationship between scanning speed and effective pulse overlap rate with diameters of 5 μm and 10 μm. From Fig. 6, the surface layer with nanopores was removed by

decreasing the scanning speed from 400 mm/s to 300 mm/s at 400 mW and from 900 mm/s to 700 mm/s at 600 mW, respectively. It was found that the nanopore formation without removal of the surface grains occurred when the pulse overlap rate was smaller than approximately 10%. When irradiated at a lower scanning speed smaller than the overlap rate of 10%, the existing nanopores were further processed by the subsequent irradiation pulses, and the removal area on the sample surface gradually increased. Therefore, low overlap is suitable for nanopore formation. Thus, nanopore generation without removal of the surface layer can be achieved by irradiating above a certain scanning speed.

3.1.3. Effect of number of scans

To examine the effect of the number of scans, line irradiation was performed on the YSZ surface at a laser power of 400 mW and a scanning speed of 1000 mm/s. The SEM images of the irradiated surface at each number of scans are shown in Fig. 8. When $N = 1$, nanopores were partially formed on the surface (Fig. 8(a)). By increasing the number of scans, the number of pores increased (Fig. 8(b)). On the other hand, when the number of scans increased, not only nanopores but also spallation of zirconia grains was generated (Fig. 8(c)). The direction of grain spallation was uniform and perpendicular to the laser polarization. The spallation is considered to have
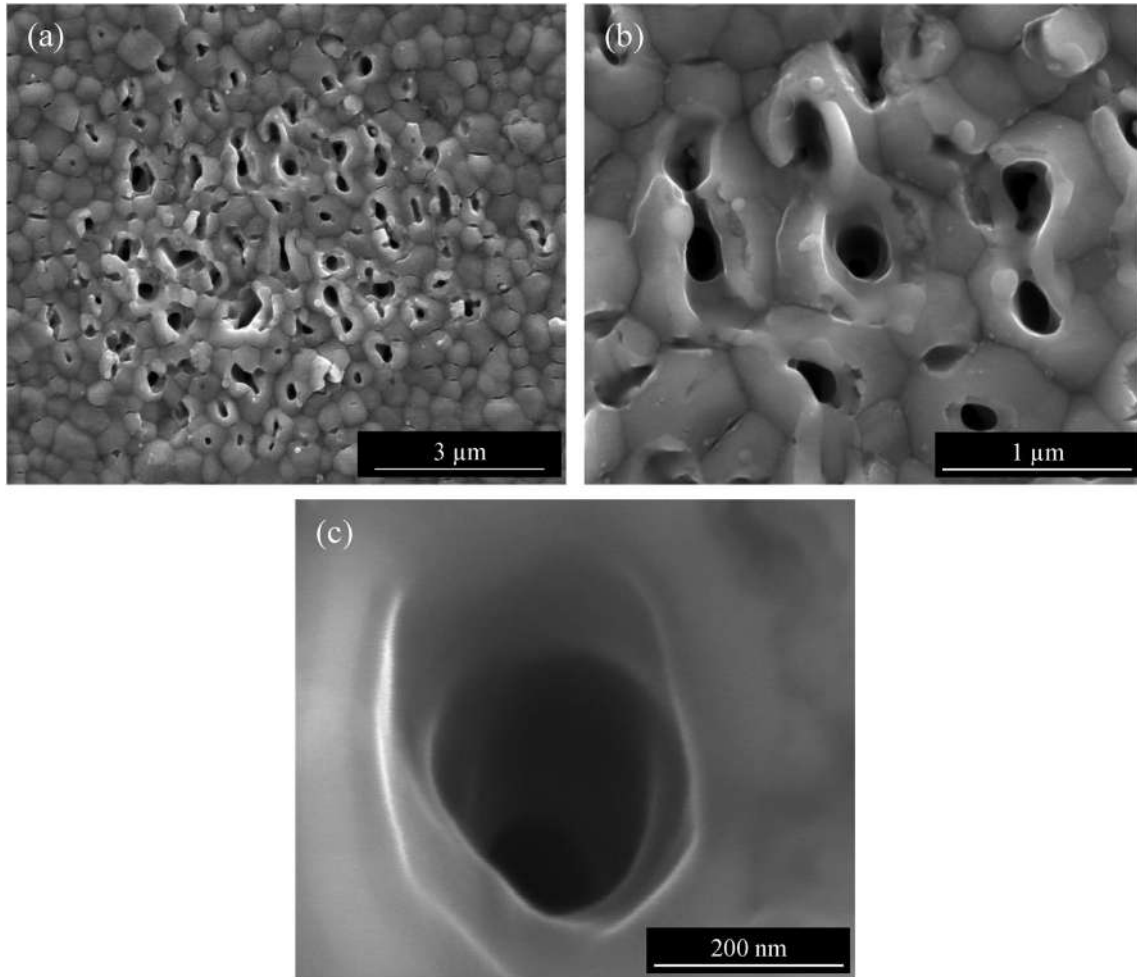
Fig. 4 — (a) SEM image of nanopores irradiated at 500 mW, (b),(c) magnified image.

been formed by thermal stress during laser irradiation. The heating mechanism in femtosecond pulsed laser processing has been studied by Taylor et al. [23] by using a numerical model. When the material is irradiated by an ultrashort pulsed laser, the surface temperature rises rapidly. After laser irradiation, the surface is rapidly cooled down with shrinkage due to thermal stress. The stress concentrates at the grain boundary, which finally results in spallation. Since this temperature change process takes place in a very short time, no thermal damage, such as phase transformation of zirconia, is expected to occur. In addition, due to the laser polarization, the interference of the incident laser beam on the material surface occurs, which causes the grain boundary to form spallation in certain directions. The multiple laser irradiation induced the generation and expansion of the gap. When $N = 5$, laser ablation occurred and a shallow microgroove formed (Fig. 8(d)). The zirconia grains on top layer were completely removed and a porous surface was observed. The porous surface formed due to the difference in laser energy absorption properties of each grain. It was found that the grains under the top layer were also removed. Fig. 9 shows the cross-sectional profiles of the machined area irradiated at a different number of scans. The ablation depth at $N = 5$ was 300—500 nm which corresponds to the diameter of one

zirconia grain. Therefore, it is considered that the YSZ surface was machined layer by layer by repeating laser scans. Moreover, once the top layer was removed and microgrooves generated, the groove depth increased with each subsequent irradiation. It is due to the increase of surface roughness which induces more laser absorption in the material. According to these results, a small number of scans is preferable for fabricating nanopores on the YSZ surface to suppress the generation of grain spallation and hinder further ablation. A parameter map for laser irradiation under a different number of scans was made to summarize the results as shown in Fig. 10. Nanopores can be generated in a small range of scanning speeds and laser power at a single time scan at $N = 1$. The range of conditions in which nanopores formed was further reduced by multiple irradiations, and no pores were formed at $N = 10$. At low power, below 300 mW, where nanopores did not form, only the grain spallation shown in Fig. 8(c) was promoted by increasing the number of scans.

3.2. Mechanism of nanopore generation

Based on the results in previous sections, nanopores can be considered to be generated by laser absorption inside the grain. The importance of the influence of surface topography
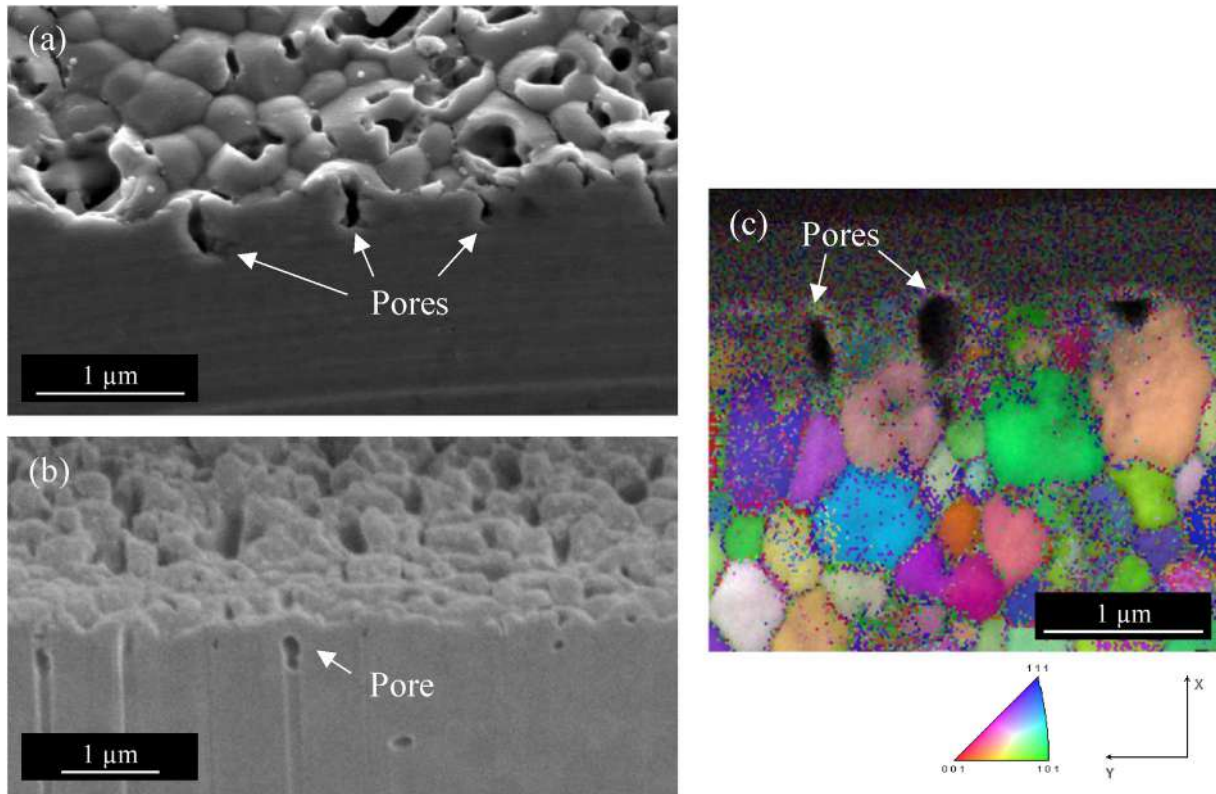
Fig. 5 — Cross-sectional images of the irradiated surface at a laser power of 500 mW: (a) SEM image of nanopores, (b) internal pore cut by FIB, (c) IPF map of nanopores.

on the processing phenomena was described in a previous study. Wang et al. [24] showed that when a nanosecond laser was irradiated onto a surface on which indium particles were placed, the temperature increased toward the apex of the sphere, and the top of each particle was preferentially processed. In this research, femtosecond pulses were used, and the pores formed were quite deep and elongated. Therefore, it is necessary to consider factors other than thermal effects, such as the behavior of the laser beam when zirconia is irradiated by the laser because the YSZ polycrystalline surface is composed of highly permeable grains and has many grain boundaries.

The top surface shape of grains exposed on the surface was measured by AFM. Fig. 11(a) and Fig. 11(b) show the three-dimensional topography of the YSZ surface and profile of grains, respectively. As the surface of grains is convex in nature, when a laser is irradiated, part of the laser beam gets reflected from the surface depending on the incident angle, while some go inside the grain. To discuss the behavior of incident light in each grain, three cases are considered: incident light passes from the air to the grain, from the grain to the adjacent grain, and from the grain to the air. Fig. 12 summarizes the change in reflectance with incidence angle in every three cases. The reflectance R when the light travels

through a material with refractive index n_1 to n_2 was calculated by using the following equation:

$$R_p = \left| \frac{n_2^2 \cos\theta - n_1 \sqrt{n_2^2 - n_1^2 \sin^2\theta}}{n_2^2 \cos\theta + n_1 \sqrt{n_2^2 - n_1^2 \sin^2\theta}} \right|^2 \tag{1}$$

$$R_s = \left| \frac{n_1 \cos\theta - \sqrt{n_2^2 - n_1^2 \sin^2\theta}}{n_1 \cos\theta + \sqrt{n_2^2 - n_1^2 \sin^2\theta}} \right|^2$$

where θ is the incident angle of light, and the subscripts p and s identify the p-polarization and s-polarization, respectively. When the light travels from the air to the grains (Fig. 12(a)), the refractive index of YSZ ($n_{grain} \approx 2.17$) is sufficiently larger than the refraction in the air ($n_{air} = 1$), and the reflectance increases gradually with increasing incident angle. When light passes through grain and moves to an adjacent grain (Fig. 12 (b)), it causes scattering and reflection at the grain boundaries. This is due to the change in refractive index at the grain boundary, which depends on the change in material density at the grain boundary and the direction of the crystal plane. When light passes between crystalline grains with
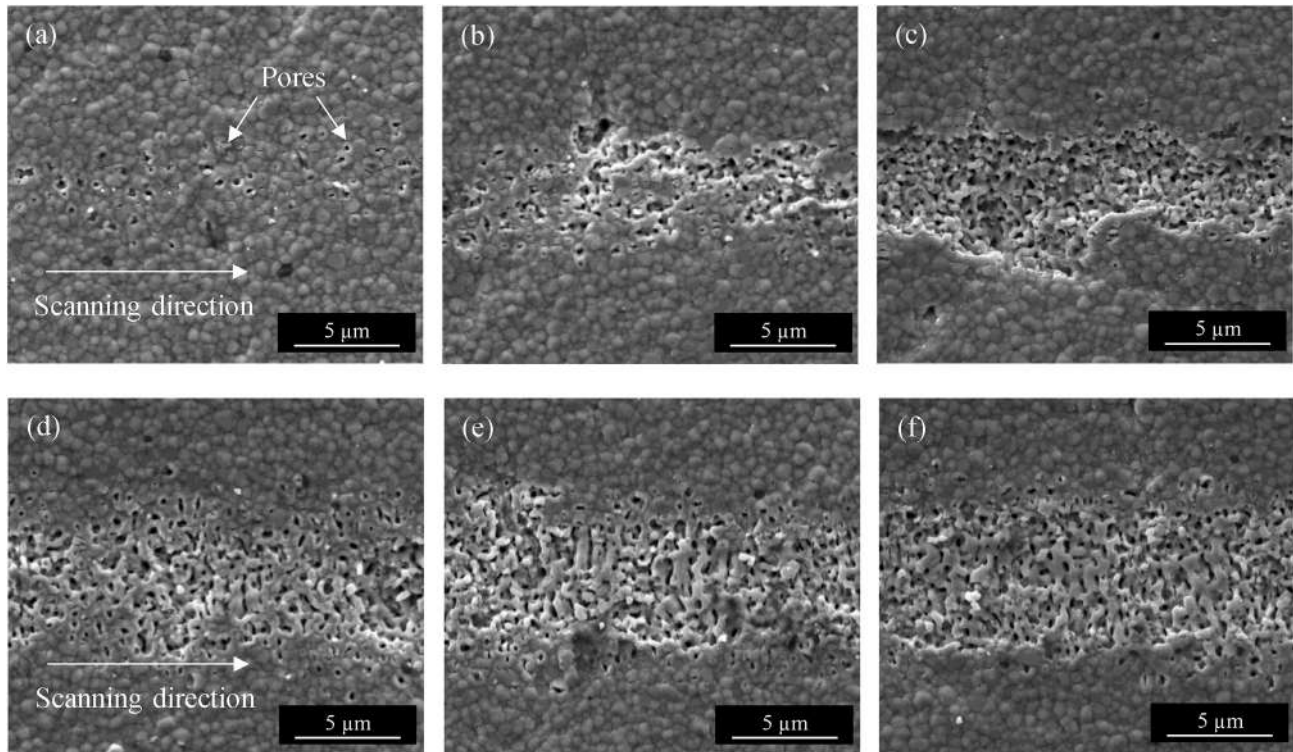
Fig. 6 − SEM images of irradiated surface under different scanning speed: (a) 400 mm/s, (b) 300 mm/s, (c) 200 mm/s are irradiated at 400 mW and (d) 900 mm/s, (e) 700 mm/s, (f) 600 mm/s are irradiated at 600 mW.

optical anisotropy, the refractive index changes depending on the direction of the crystal plane, so the effect of grain boundaries is particularly large as zirconia is a polycrystalline material. In addition, Boulouz et al. [25] reported that, at the grain boundary, the refractive index decreases with increasing yttria concentration due to the dopant segregation, and the refractive index is assumed to decrease by about 0.1 for a few mol% increase in yttria concentration that may

occur at grain boundaries. Hence, total reflection occurs above the critical angle. When the light passes from grain to air (Fig. 12(c)), total reflection of lights easily occurs, and lights do not go out into the air because of the large difference in refractive index ($n_{grain} \gg n_{air}$).

Considering the zirconia sample as a cross-section of a sphere as shown in Fig. 13(a), a phenomenon during laser irradiation can be inferred as follows. On the convex surface,
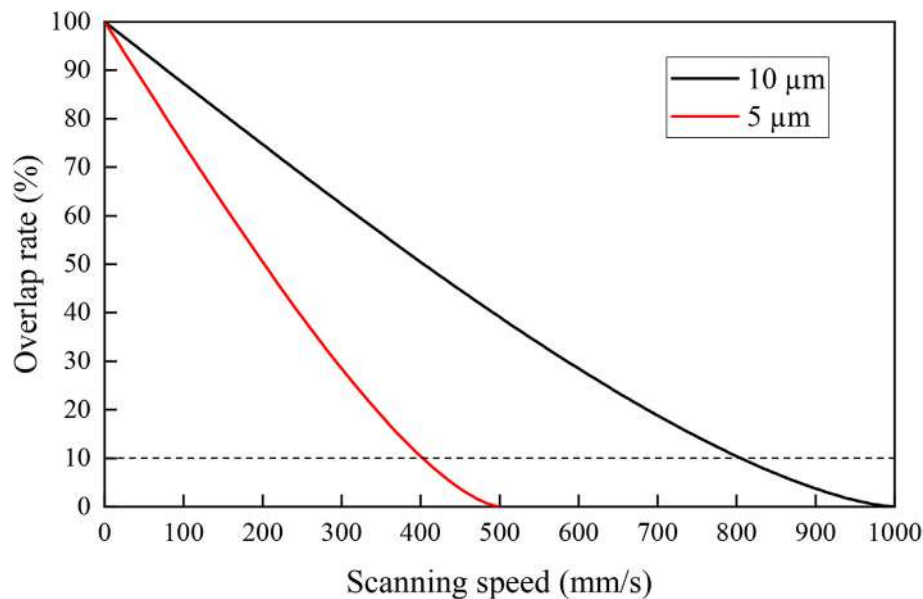

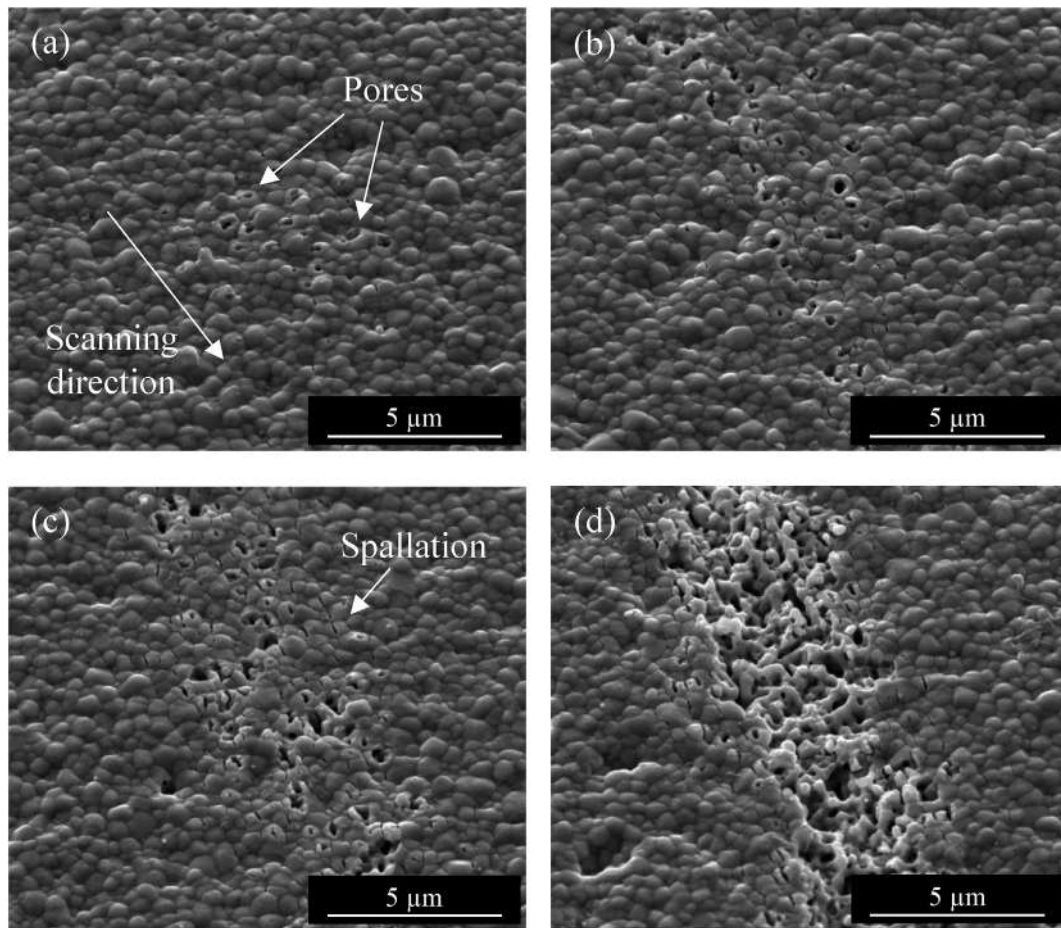**Fig. 7 − Laser pulse overlap change with scanning speed.**

Fig. 8 − **SEM images of the irradiated surface under a different number of scans taken at a 30-degree angle: (a) N = 1, (b) N = 2, (c) N = 3, and (d) N = 5.**
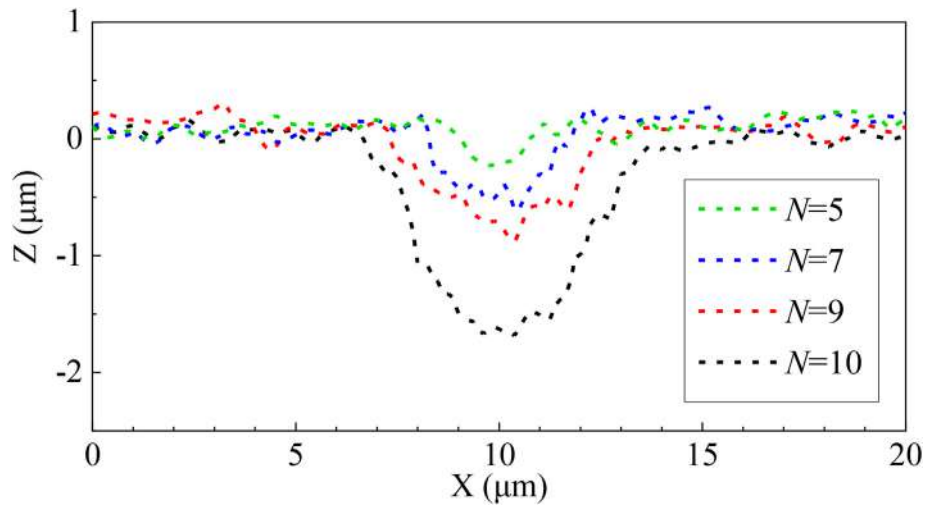

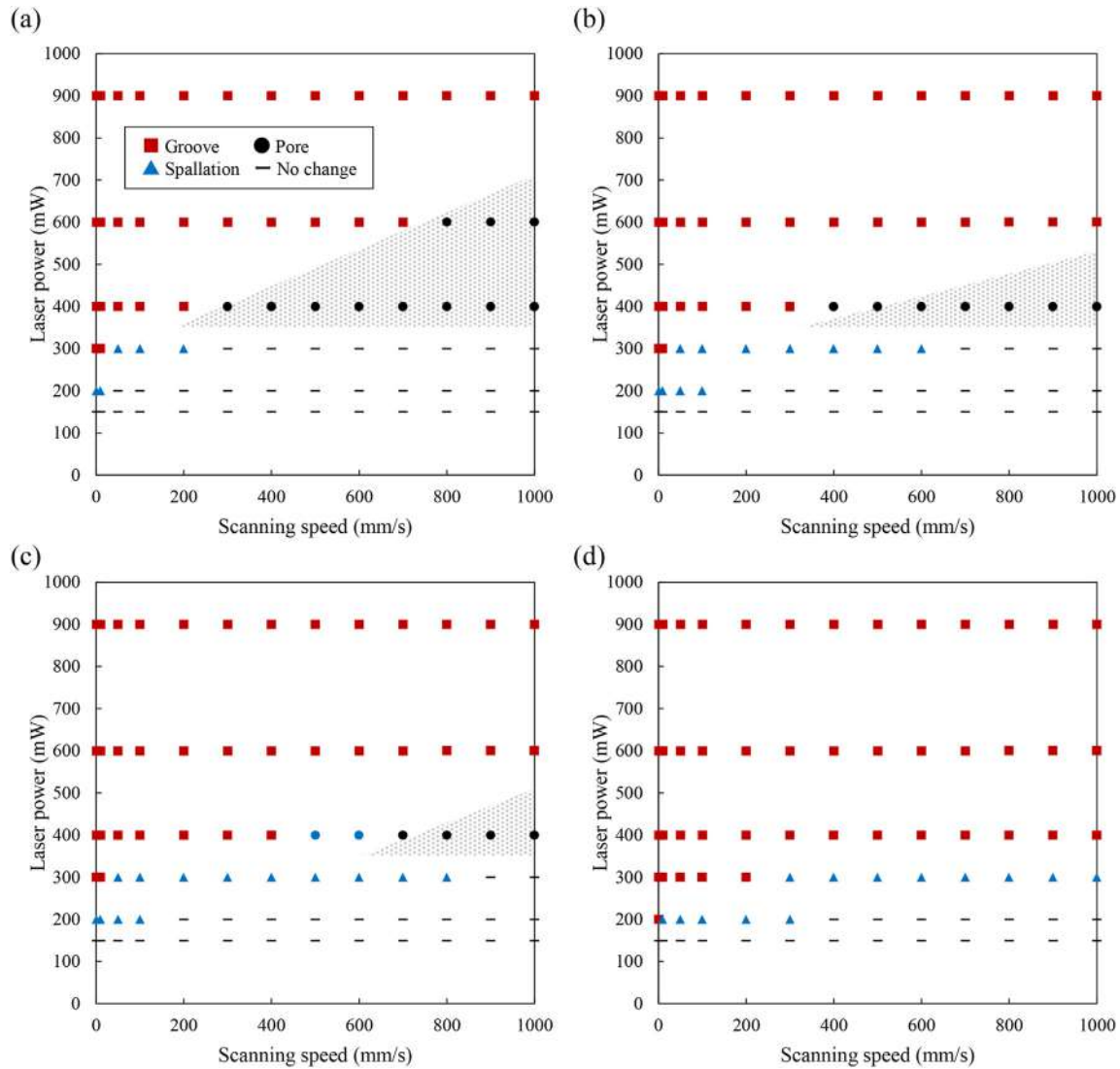**Fig. 9** − **Cross-sectional profiles of microgrooves irradiated under different number of scans.**

Fig. 10 − Parameter map of surface structures irradiated at the different number of scans: (a) N = 1, (b) N = 2, (c) N = 3, (d) N = 10.

the incident laser of intensity I_0 is reflected and scattered at the interface depending on the incident angle, and only the laser of intensity I_{in} shown in the following equation goes inside.

$$I_{in} = (1 - R)I_0 \tag{2}$$

As zirconia has a high refractive index, the laser entering the grain is focused inside the zirconia grain like a lens. From the surface profile (Fig. 11(b)), each grain is approximated by a circle, and focal length l is calculated by using the following equation:

$$l = \frac{r}{n - 1} \tag{3}$$

where r is the radius of curvature. Since aberrations occur in a lens, the minimum circular diameter of the energy focused region, d_a, is given as follows:

$$d_a = K\frac{D^3}{l^2} \tag{4}$$

$$K(n) = \left| -\frac{n(4n - 1)}{16(n - 1)^2(n + 2)} \right| \tag{5}$$

where D is the diameter of the lens. The laser fluence F at the area is calculated by the following equation.

$$F = \frac{I_{in}}{\text{Area}} = \frac{4I_{in}}{\pi d_a^2} \tag{6}$$

The results of these calculations are shown in Table 2. Five grains measured by AFM as shown in Fig. 11(b) were extracted for evaluation. It was found that some of them had a minimum diameter smaller than 100 nm. In this experiment, the fluence used to generate nanopores was very small and near the ablation threshold (1.27 J/cm² at 400 mW), but
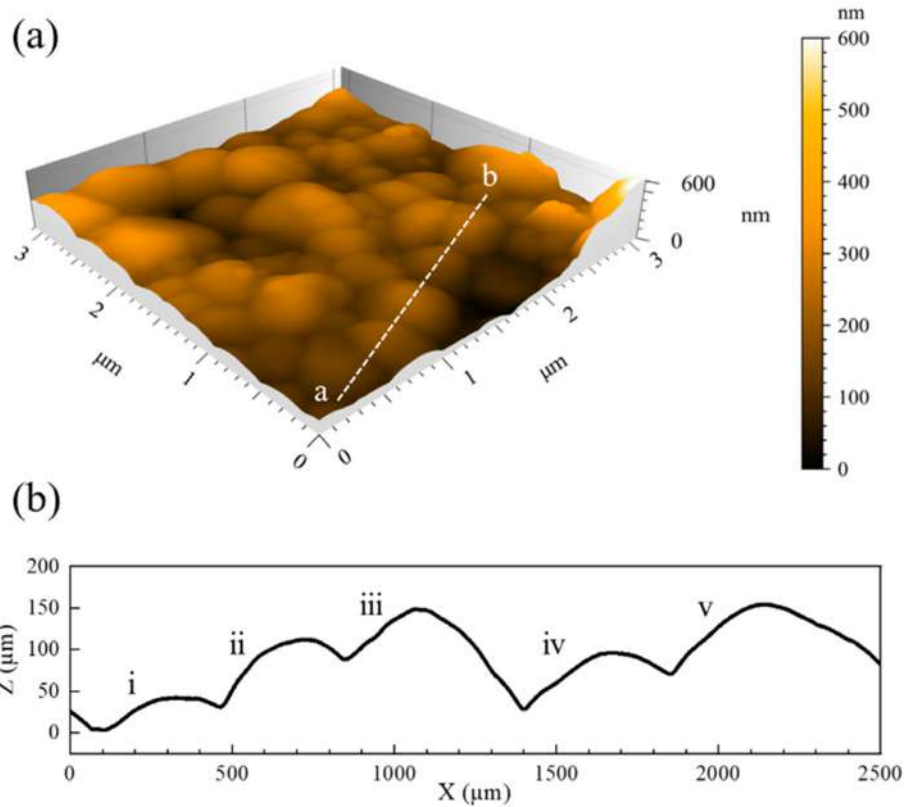
Fig. 11 − (a) Three-dimensional topography of the YSZ surface measured by AFM (b) cross-sectional profile in (a).
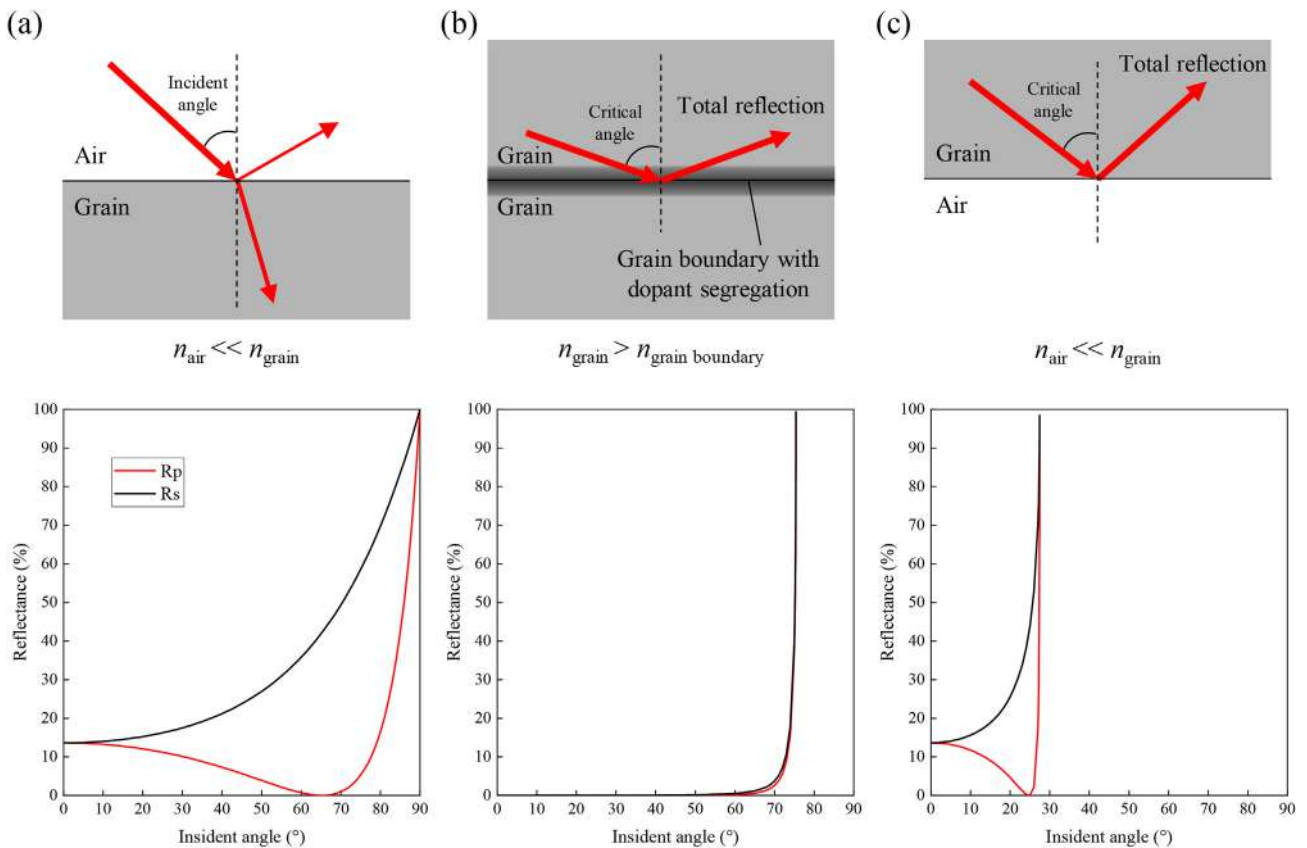

Fig. 12 − Change in reflectance with incidence angle and schematic drawings in three cases: incident light passes (a) from the air to the grain, (b) from the grain to the adjacent grain, (c) from the grain to the air.
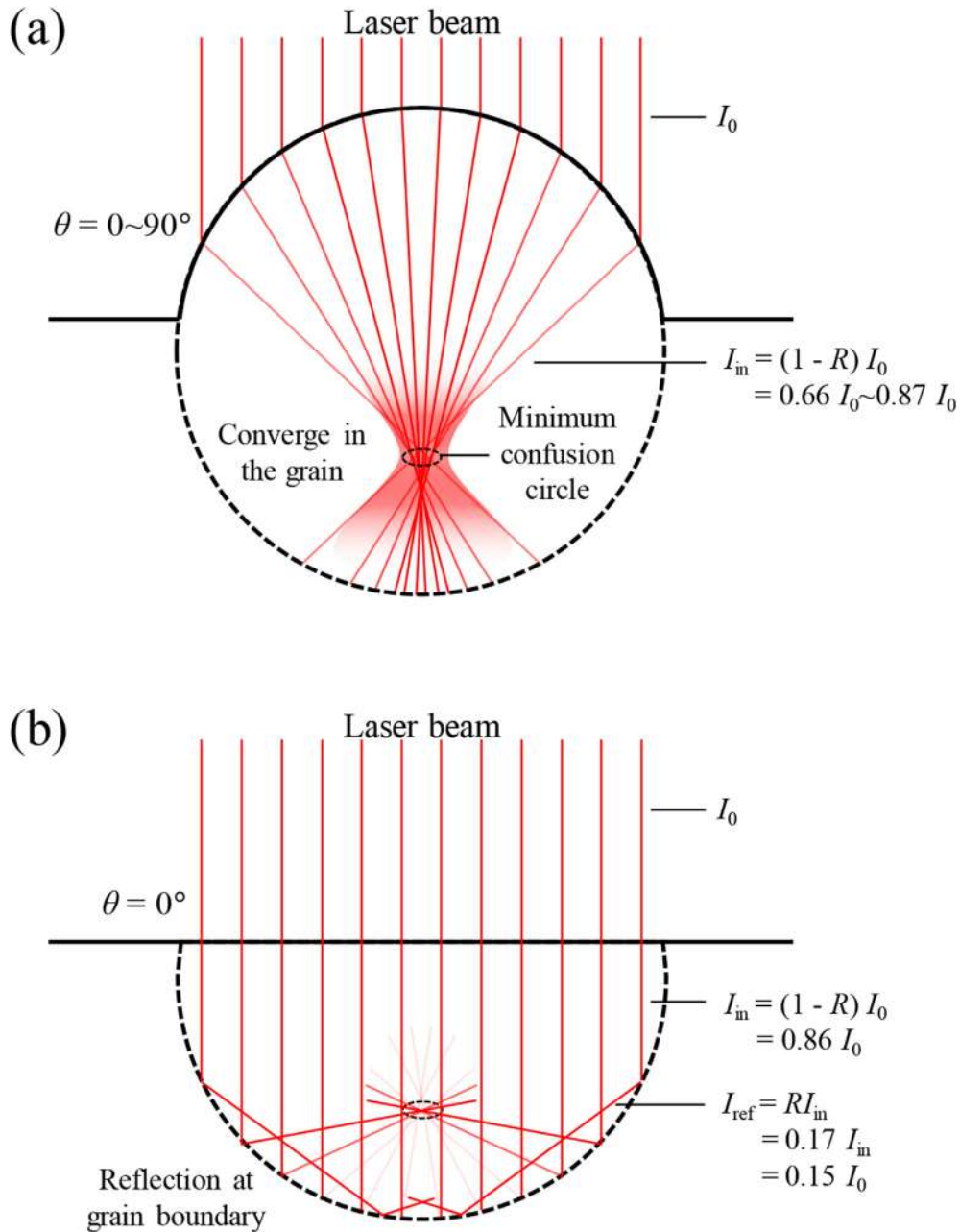
Fig. 13 − Difference in laser irradiation behavior when the grain of the top surface is (a) convex and (b) flat.

it's thought that the fluence significantly increased inside some grains during laser irradiation. This resulted in a significant increase in locally absorbed laser energy. Ablation

Table 2 − Calculated results for each value at the laser condense area within each grain when irradiated at 400 mW.

Grain	r [nm]	l [nm]	d_a [nm]	F [J/cm^2]
i	634	542	23.9	132−175
ii	424	363	78.5	12.3−16.3
iii	489	418	176	2.46−3.25
iv	639	546	59.9	21.1−28.0
v	743	635	164	2.83−3.75

occurs in the region and small cavity forms inside the material. A small cavity expands by high-pressure plasma/vapor inside the grain. Then the cavity reaches the top of the grain, and the plasma/vapor is ejected into the atmosphere and a pore remains inside the material. As a result, pores are formed in the grains of the top layer by single time laser irradiation as described in Fig. 3. The long-elongated pores formed are thought to be the result of energy absorption in the elongated region due to laser aberration inside the grain. Thus, even at wavelengths that are not efficiently absorbed by zirconia (zirconia is transparent to the wavelength), if the laser beam is locally intensified due to lens effect, the laser intensity reaches a certain threshold where laser can effectively be absorbed leading to ablation. It was reported that
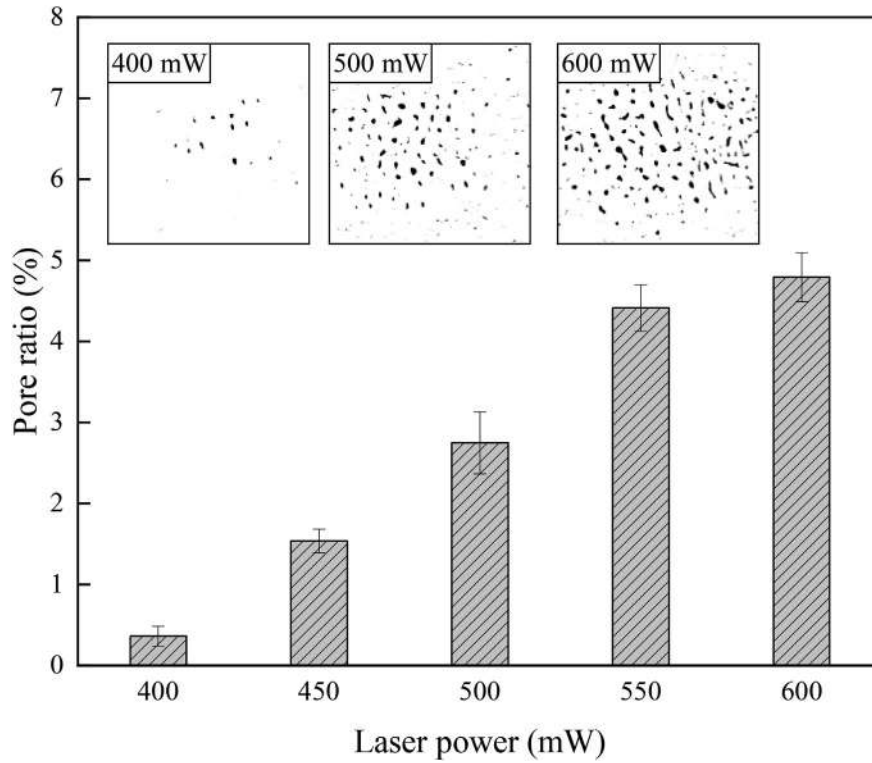
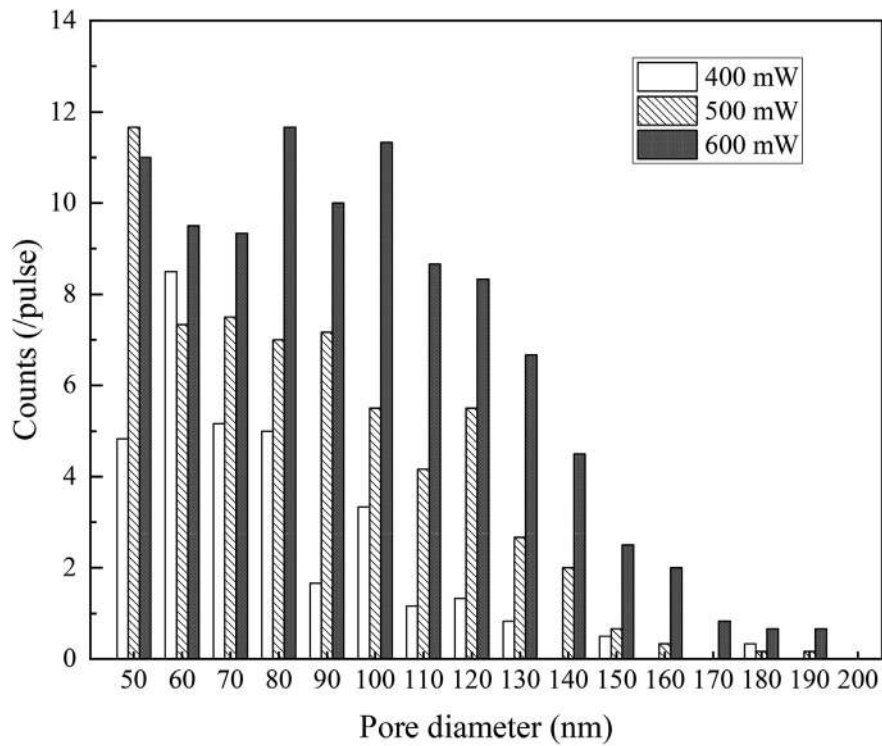**Fig. 14 — Change in pore ratio with laser power.**

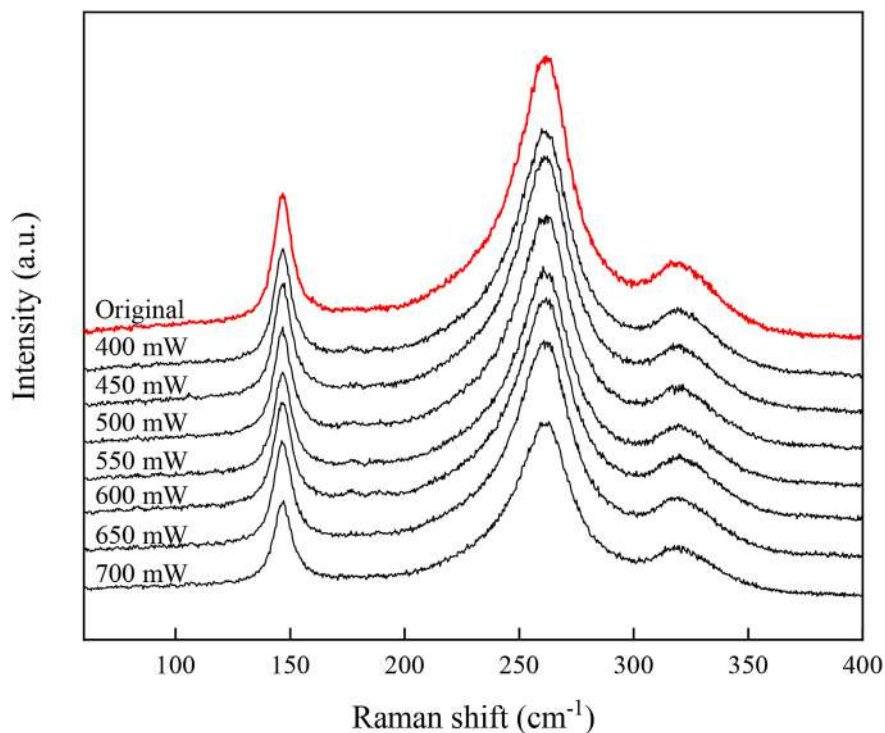**Fig. 15 — Change in pore diameter with laser power.**

Fig. 16 — Raman spectra of the irradiated surface under various laser power (scanning speed 1000 mm/s, N = 1).

peak intensity is the most important factor and even if the number of irradiation or pulse overlap is increased, significant material ablation will not occur if the intensity of a single pulse is not high enough to develop an efficient process for laser absorption [26]. These results explain the formation of nanopores with only one shot of pulse irradiation by controlling laser parameters in this study.

Fig. 13(b) shows the case where the surface is not convex but flat. The incident light passes through the material. As mentioned before, some total internal reflection occurs at the grain boundaries. The reflected beams are concentrated near the center of the bottom of the grain, and energy absorption occurs. However, the intensity of the reflected light is extremely low. Therefore, it is considered that pore is more likely to form in the convex grain.

In the actual YSZ sample, the grains are not perfect circles. The cross-sectional observation results, shown in Fig. 5(c), show that the internal grain shapes are of various sizes and shapes. Therefore, the behavior of the light changes depending on the incident angle change at both upper and lower surfaces of the grain. In this way, even when the surface is irradiated once, there are differences in the ease of light focusing and the position of the light focus within the grain, resulting in some grains having pores and others not. In addition, if the beam is concentrated in the too deep region, a laser-induced cavity will not reach the surface and it will remain inside the grain with the grain expanding slightly by internal pressure, as mentioned in Fig. 5(b).

Based on the above mechanism, the effect of each laser irradiation condition is considered as below. When the laser power increases, the peak intensity increases, which promotes more energy absorption, and more nanopores are generated. The difference in pore size within a pulse, referred to in Fig. 3, is because of the Gaussian energy distribution of the laser beam. As the energy intensity increases in the center of the beam, more ablations occur in the grains, resulting in a larger pore formation. In addition, when the pore diameter reaches the YSZ grain size by increasing the laser power, the neighboring pores bond with each other to form larger pores. Furthermore, the pulse overlap rate changes by changing the scanning speed. As the overlap rate increases, the number of pulses irradiated per unit area increases. Existing pores are further processed, and cavities under the surface are increased and enlarged by repeated energy absorption. As a result, the formation of pores is promoted under the surface and the grains in the surface layer are removed, which leads to the microgrooving process.

3.3. Pore size analysis

For quantitative analysis of nanopore fabrication, the pore ratio of the laser irradiated surface at a scanning speed of 1000 mm/s with different laser power was evaluated. In general, the porosity of porous materials is calculated as the volume fraction of pores per unit volume. However, as seen in the cross-sectional observation results, pores were formed only in the top layer of the sample, so in this study, the pore ratio was calculated as the area fraction of pores per laser irradiated area (10 μm × 10 μm). Fig. 14 shows how the pore ratio changes with the laser power. As the laser power increased, the pore ratio also increased linearly. This is because the number of nanopores formed in a single laser
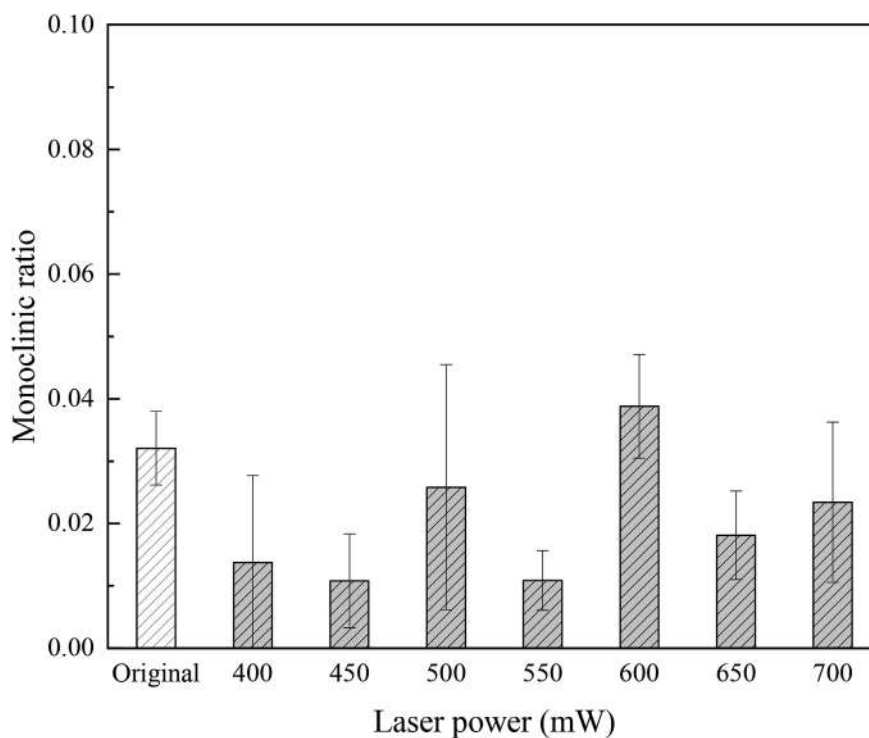
Fig. 17 — Change in monoclinic ratio with laser power.

pulse increased almost linearly due to the effective size of the laser spot for pore formation increasing depending on the laser power, corresponding to the results shown in Fig. 3. For detailed investigation, the diameters of the individual pores at each laser power were calculated. Fig. 15 shows the change in the distribution of nanopore diameters with various laser power. The sample originally contained residual pores less than 50 nm in diameter at grain boundaries which were
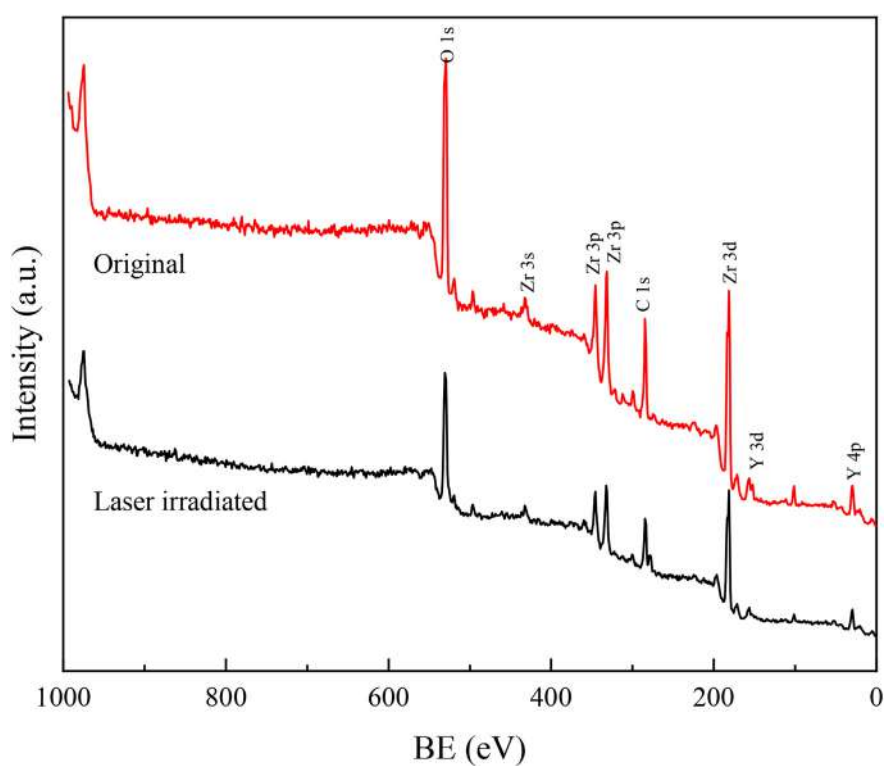

Fig. 18 — XPS spectra of YSZ surfaces before and after irradiation.
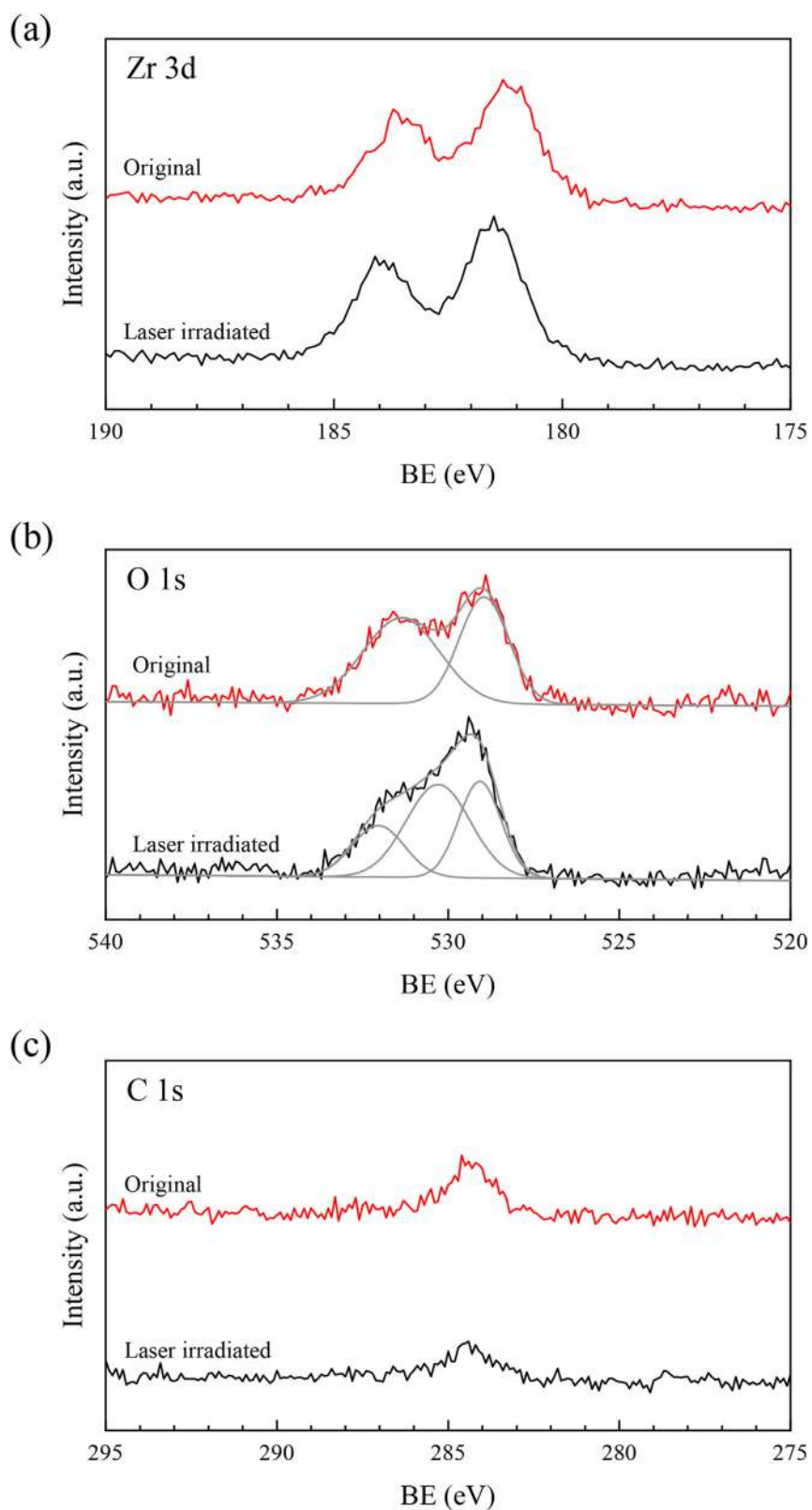
Fig. 19 − XPS spectra of YSZ surfaces before and after irradiation for each element.

generated during the sintering process of the ceramic. To distinguish laser-machined pores from them, a cutoff diameter value of 50 nm was used. As the laser power increased, the pore diameter shifted to larger values. In addition, the

higher laser power showed a larger number of pores. At higher laser power (600 mW), pores were formed in the entire range of 50−200 nm and the maximum pore diameter value was about 190 nm. On the other hand, at lower laser power

(400 mW), there were almost no pores in the range of 150 nm−200 nm. It can be hypothesized that the amount of material removed from the zirconia grains increased due to the increase in absorbed energy caused by the increase in incident laser power, which means the pore diameter became wider. Moreover, it is because that the diameter of the pores increased because neighboring pores combined to form larger pores when increasing laser power.

3.4. Material phase analysis

To detect possible phase transformation of YSZ during laser machining, the Raman spectra of the sample were measured. Fig. 16 presents the Raman spectra of the machined surface irradiated at 1000 mm/s and N = 1 with various laser power. Before and after laser irradiation, two tetragonal peaks (147 cm^{-1} and 264 cm^{-1}) appeared on the YSZ surface in all conditions. No clear monoclinic peaks (181 cm^{-1} and 190 cm^{-1}) were observed between the tetragonal peaks. In general, the tetragonal phase of YSZ transforms to the monoclinic phase due to temperature change during laser irradiation. However, in this study, the monoclinic peak intensity did not increase significantly after laser irradiation. This indicates that the thermal effect of laser irradiation is small and the tetragonal phase is still dominant in the irradiated surface. In our previous study, samples in which no clear increase in the monoclinic peaks was observed, the quantitative analysis for the monoclinic ratio confirmed the existence of a monoclinic phase of 0−10% based on the calculation results [19]. Therefore, quantitative analysis is an effective method to evaluate phase transformation after laser irradiation in detail.

For quantitative analysis, the Raman intensity method was used by Muñoz Tabares and Anglada [27] to calculate the monoclinic volume ratio. The minimum points of each peak of the Raman spectra were connected to determine the baseline. Then, the integrated intensity I from the baseline was measured for three peaks, and the monoclinic ratio V_m was calculated by substituting into the following Eq. (7).

$$V_m = \frac{I_m(181) + I_m(190)}{2.07 \times I_t(147) + I_m(181) + I_m(190)} \qquad (7)$$

where the subscripts m and t identify the monoclinic and tetragonal phases, respectively, and the numbers in parentheses indicate the wavenumber of the peak. Fig. 17 shows the change in the calculated monoclinic ratio. The monoclinic ratio of the original surface was approximately 3%, as the YSZ substrate originally contained a small amount of monoclinic phase. After laser irradiation, the monoclinic ratio randomly ranged from 1 to 4%, and quite a big measurement error was found. There was no significant increase or decrease in the monoclinic ratio compared to the original surface, and there was no correlation between laser power and monoclinic ratio. In our previous study, an increase in the monoclinic phase was observed after femtosecond laser irradiation at higher laser power (about 900 mW) [19]. This result indicates that a low laser power near the ablation threshold does not affect the phase transformation during nanopore fabrication.

3.5. Surface chemistry analysis

The surface chemistry of YSZ before and after laser irradiation was analyzed. The sample with nanopores was prepared by area irradiation with a laser power of 500 mW, a scanning speed of 1000 mm/s, a scan pitch of 8 μm, and the number of scans was 1. Figs. 18 and 19 show the results of the XPS analysis. For the XPS spectra shown in Fig. 18, mainly Zr, O, Y, and C peaks were detected, which were consistent with the composition of the YSZ sample. These constituent elements did not change before or after the laser irradiation. For the spectra of each element (Fig. 19(a)−(c)), there was no significant change apparent in the shape of the Zr 3d and C 1s peaks. On the other hand, the O 1s peak showed two distinct peaks at around 530 eV, and the peak shape changed after laser irradiation. The peak at 530 eV indicates the binding energy of oxide (Zr−O), the peak at 531 eV indicates the binding energy of oxide with an oxygen vacancy (Zr-O$_{vac}$) [28], and the peak at 532 eV indicates the binding energy of hydroxide (Zr−OH) [29]. The peak-fitting analysis identified an oxygen vacancy peak between the two peaks corresponding to 530 and 532 eV after laser irradiation. Therefore, it can be concluded that an oxygen vacancy was generated at the surface after the nanopore generation. In YSZ, Zr^{4+} is replaced by Y^{3+} with a different valence. To compensate for the charge imbalance created inside the material, oxygen vacancies are placed around the dopant elements (yttria) in the lattice. Thus, original zirconia should also have an oxygen vacancy, however, the concentration of oxygen vacancies highly depends on the dopant concentration. YSZ used had a small amount of yttria (3 mol%), and the Y element was known to accumulate in the region near the grain boundary [30]. XPS analysis can evaluate elements only present a few nanometers below the sample surface. The grain size of the YSZ sample used in this study was a few hundred nanometers scale. Thus, it can be considered that the number of vacancies might not be sufficient to be analyzed, Bayati et al. could not observe oxygen vacancies in cubic zirconia, which have significantly more oxygen
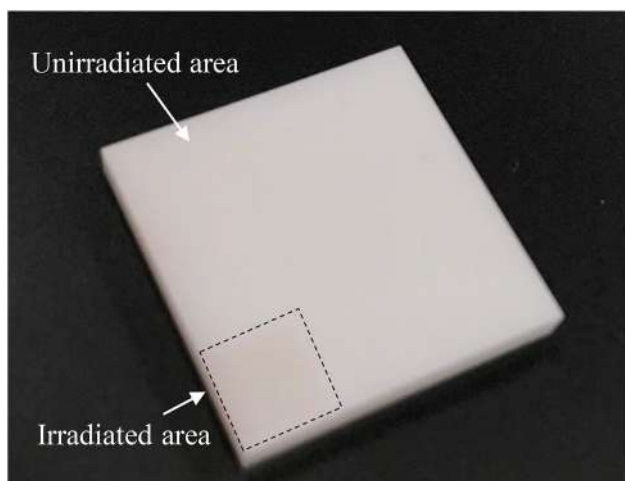

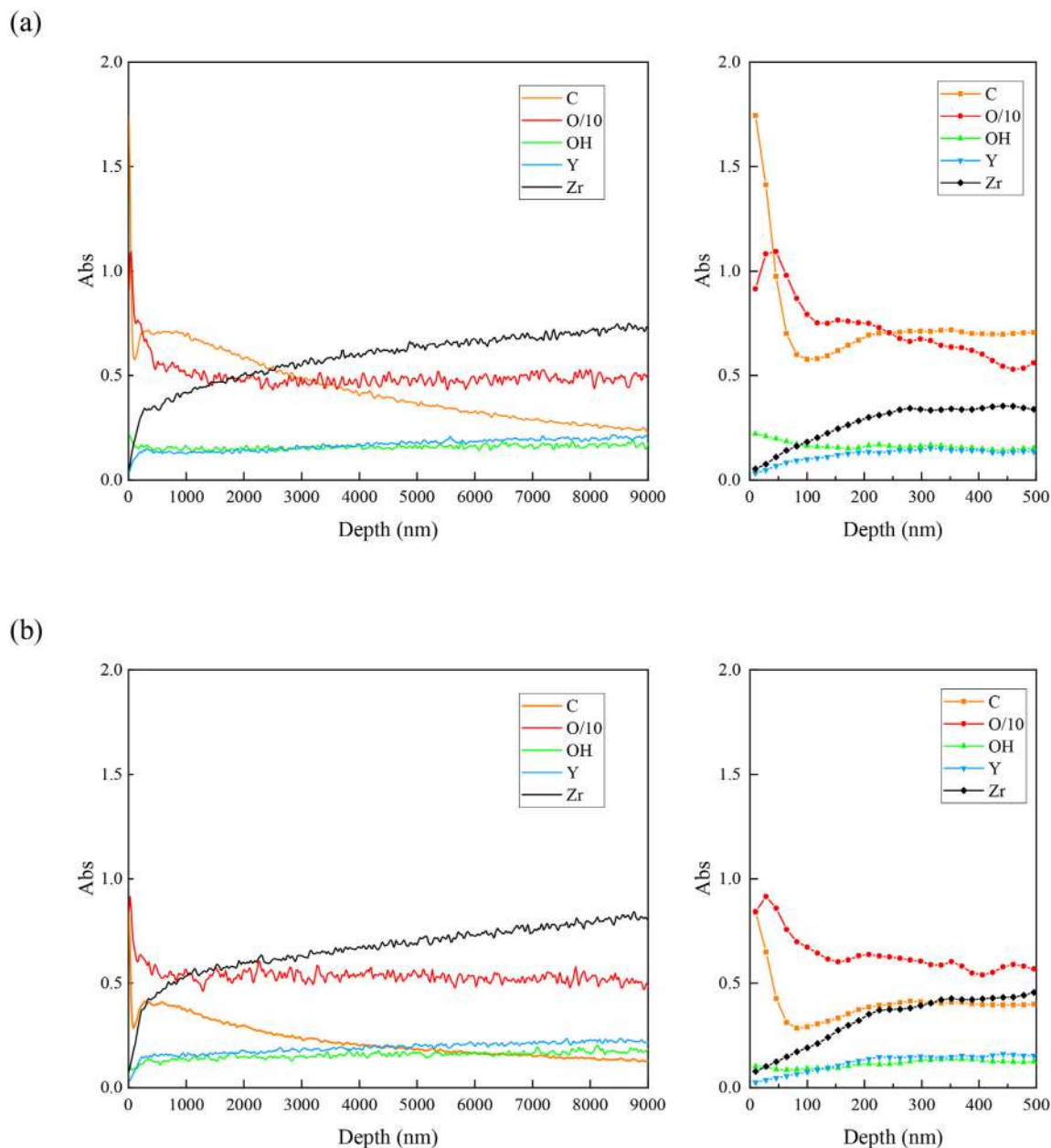**Fig. 20 − Overview of YSZ sample after laser irradiation.**

(a)

(b)

Fig. 21 − GDOES analysis: (a) before laser irradiation, and (b) after laser irradiation.

vacancy as compared to tetragonal zirconia [31]. After laser irradiation, a clear oxygen vacancy peak was observed. This means that a sudden oxygen defect occurred at the topmost surface of the sample after laser irradiation. During the laser process, the oxygen partial pressure in the atmosphere decreases instantaneously. Oxygen ions in the lattice are then released as oxygen gas, leaving vacancies and electrons. The following reaction occurs, resulting in an increase of oxygen vacancies (V_O) in the sample surface [32].

$$O \rightarrow 1/2O_2 + V_O + 2e^- \qquad (8)$$

The excess electrons produced in this reaction reduce some of the zirconium ions to form oxygen-deficient zirconia with a large number of oxygen vacancies.

As shown in Fig. 20, the laser irradiated area was discolored and slightly reddish compared to the unirradiated area. In general, darkening occurs when zirconia is irradiated by a laser [33]. This is due to the laser-induced internal defects in the material, and it can be said that free carriers bound to oxygen vacancies in the lattice caused the formation of color centers that absorb light of specific wavelengths. Hence, in this study, the color center was formed due to the generation of an oxygen vacancy by laser irradiation which changed the sample color. The redness disappeared as time passed after the laser irradiation and returned to the original white color.

GDOES analysis was performed to investigate the surface property in detail. Fig. 21 shows the change in the amount of each chemical component with depth from the sample surface. After laser irradiation, the carbon (C) on the top layer

(~50 nm) has decreased. Since the amount of carbon significantly decreased in the interior of the material, the carbon was the organic matter attached to the surface of the material. The sample was cleaned with ethanol before laser irradiation, so it can be said that the laser irradiation removed microscopic organic matter by the surface cleaning effect. In addition, no significant changes in other components such as zirconium (Zr), yttrium (Y), and oxygen (O) were observed before and after the laser irradiation. The nanopore generation by femtosecond laser irradiation hardly changed the chemical composition of the YSZ surface, and only the attached organic matter was removed.

3.6. Surface wettability evaluation

As an example of evaluation of the surface property with nanopores, surface wettability was investigated. The nanopores were generated on the entire YSZ surface by area irradiation with a laser power of 500 mW, scanning speed of 1000 mm/s, scan pitch of 8 μm, and the number of scans was 1. Fig. 22 shows images of the water droplets on the original and irradiated surface, with an optical microscope image of the machined surface below. The original YSZ surface before laser irradiation had an intrinsic contact angle of about 73°, indicating the surface was hydrophilic. The surface with nanopores showed a decrease in contact angle and improvement in hydrophilicity. Contact angle change with different laser power is summarized in Fig. 23. When irradiated at 500 mW, the contact angle decreased, but at 400 mW, there was almost

no change in the angle and the angle was similar to that of the original surface. This indicates that wettability can be changed by the pore ratio of the irradiated surface, and a higher pore ratio surface presents more hydrophilicity. The optical microscope image in Fig. 22 shows that the pores did not completely form over the entire surface, and there were gaps between laser pulses where no pores exist. The hydrophilicity would be further improved if the pores were fabricated entire surface.

In general, surface wettability is highly dependent on both physical surface topography and chemical properties. In the case of the topography effect, surface wettability conditions can be generally explained by two states: in the Wenzel state, the liquid penetrates the structures, and the contact area between the liquid and substrate increases. The wettability of the original sample surface is enhanced, and hydrophilic surfaces become more hydrophilic and hydrophobic surfaces become more hydrophobic [34]. In the Cassie-Baxter state, the contact area decreases due to air pockets generated at the liquid-solid interface [35]. In this study, the nanopores have led to hydrophilicity, attributed to the dominance of the Wenzel state. In the case of the chemical effect, it is known that the chemical condition on the surface significantly influences wettability. Zhang et al. [36] reported that the adhesion of organic matter to the material increases surface hydrophobicity. During nanopore formation, organic matter on the YSZ was removed by laser irradiation, as mentioned in Fig. 21. Therefore, it is considered that the removal of organic matter from the sample
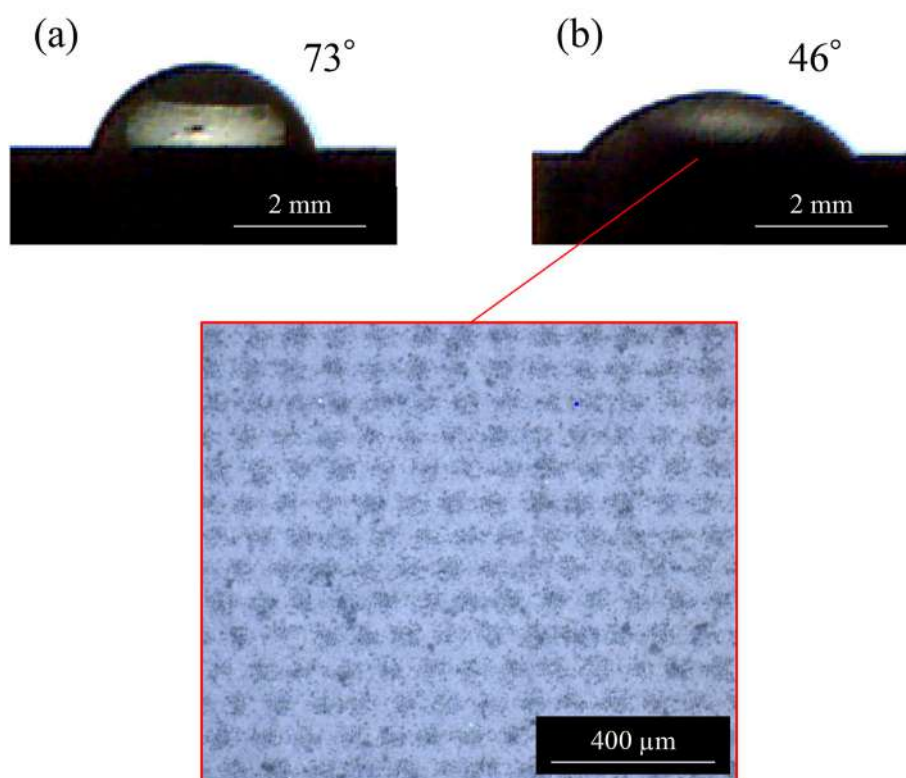

Fig. 22 — Water droplets on unirradiated and nanopore surfaces irradiated at a laser power of 500 mW: (a) original surface, and (b) nanopore surface.
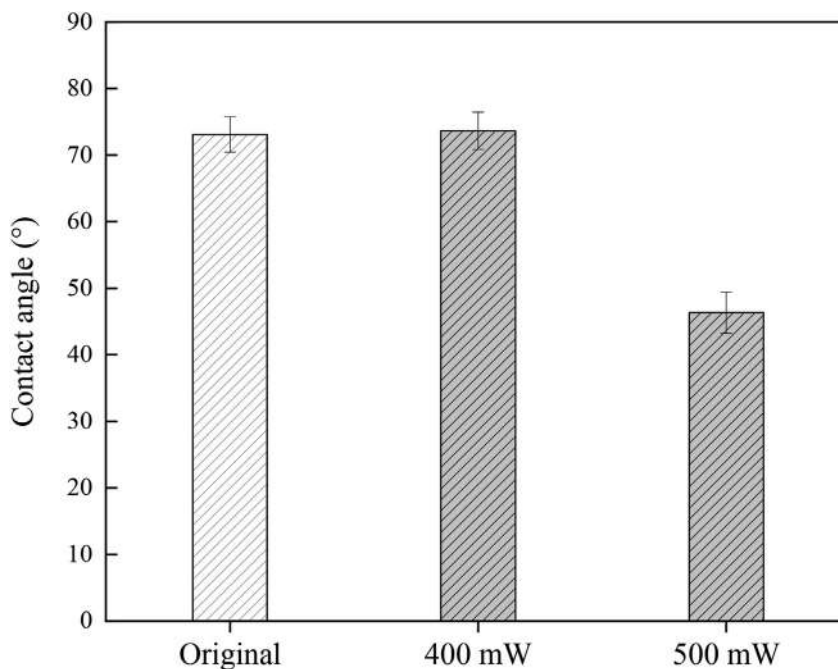
Fig. 23 − **Change in contact angle on unirradiated and nanopore surfaces irradiated at different laser power.**

surface changed the wettability and made the surface more hydrophilic in this study. However, the change in wettability is greatly affected by both the surface topography and the chemical properties. Thus, it can be said that the wettability change of the surface after nanopore generation was achieved by both the shape impartation by the nanopore and the removal of organic matter.

4. Conclusions

This study presents the possibility of nanopore generation on YSZ by femtosecond pulsed laser irradiation and its fundamental processing characteristics were investigated. The following conclusions were obtained.

(1) Nanopores with a diameter of around one hundred nanometers were generated at a limited range of laser power near the ablation threshold. The number and the diameter of the nanopores increased when increasing the laser power. Cross-sectional observation showed that the nanopores formed only in the zirconia grains of the top layer. The depth of the pores was around 500 nm.

(2) The nanopore generation mechanism involves light focusing by the convex shape of a crystal grain and ablation inside the grain.

(3) A higher scanning speed whose pulse overlap rate was lower than 10% and a lower repetition number of scans resulted in the formation of individual clear pores, preventing the removal of the top layer.

(4) The thermally induced phase transformation from the tetragonal to the monoclinic phase was not observed on the irradiated surface after nanopore generation when using femtosecond pulses due to the low laser power near the ablation threshold.

(5) The surface hydrophilicity of the YSZ was improved by fabricating nanopores due to the structural change and removal of surface organic matter.

This study demonstrated the possibility of the functionalization of YSZ surfaces by selectively generating nanopores on the top layer by using femtosecond pulsed laser irradiation without causing thermal damage to the bulk. These findings not only promote the scientific understanding of the interaction between laser light and polycrystalline materials, but also provides possibility of enhancing the surface functionality such as wettability, biocompatibility, and nanomedicine delivery.

Data availability statement

The raw/processed data required to reproduce these findings cannot be shared at this time due to technical or time limitations.

Declaration of competing interest

The authors declare that they have no known competing financial interests or personal relationships that could have appeared to influence the work reported in this paper.

Acknowledgments

REFERENCES

[1] Garvie RC, Hannink RH, Pascoe RT. Ceramic steel? Nature 1975;258:703–4. https://doi.org/10.1038/258703a0.

[2] Piconi C, Maccauro G. Zirconia as a ceramic biomaterial. Biomaterials 1999;20:1–25. https://doi.org/10.1016/S0142-9612(98)00010-6.

[3] Hou PJ, Ou KL, Wang CC, Huang CF, Ruslin M, Sugiatno E, et al. Hybrid micro/nanostructural surface offering improved stress distribution and enhanced osseointegration properties of the biomedical titanium implant. J Mech Behav Biomed Mater 2018;79:173–80. https://doi.org/10.1016/j.jmbbm.2017.11.042.

[4] Salou L, Hoornaert A, Stanovici J, Briand S, Louarn G, Layrolle P. Comparative bone tissue integration of nanostructured and microroughened dental implants. Nanomedicine 2015;10:741–51. https://doi.org/10.2217/nnm.14.223.

[5] Chen F, Zhang D, Yang Q, Yong J, Du G, Si J, et al. Bioinspired wetting surface via laser microfabrication. ACS Appl Mater Interfaces 2013;5:6777–92. https://doi.org/10.1021/am401677z.

[6] Yao L, He J. Recent progress in antireflection and self-cleaning technology − from surface engineering to functional surfaces. Prog Mater Sci 2014;61:94–143. https://doi.org/10.1016/j.pmatsci.2013.12.003.

[7] Ji M, Xu J, Chen M, El Mansori M. Enhanced hydrophilicity and tribological behavior of dental zirconia ceramics based on picosecond laser surface texturing. Ceram Int 2020;46:7161–9. https://doi.org/10.1016/j.ceramint.2019.11.210.

[8] Losic D, Simovic S. Self-ordered nanopore and nanotube platforms for drug delivery applications. Expet Opin Drug Deliv 2009;6:1363–81. https://doi.org/10.1517/17425240903300857.

[9] Yan J, Okuuchi T. Chip morphology and surface integrity in ultraprecision cutting of yttria-stabilized tetragonal zirconia polycrystal. CIRP Ann 2019;68:53–6. https://doi.org/10.1016/j.cirp.2019.04.050.

[10] Holthaus MG, Twardy S, Stolle J, Riemer O, Treccani L, Brinksmeier E, et al. Micromachining of ceramic surfaces: hydroxyapatite and zirconia. J Mater Process Technol 2012;212:614–24. https://doi.org/10.1016/j.jmatprotec.2011.06.007.

[11] Lu A, Gao Y, Jin T, Luo X, Zeng Q, Shang Z. Effects of surface roughness and texture on the bacterial adhesion on the bearing surface of bio-ceramic joint implants: an in vitro study. Ceram Int 2020;46:6550–9. https://doi.org/10.1016/j.ceramint.2019.11.139.

[12] Scott HG. Phase relationships in the zirconia-yttria system. J Mater Sci 1975;10:1527–35. https://doi.org/10.1007/BF01031853.

[13] Gupta TK, Lange FF, Bechtold JH. Effect of stress-induced phase transformation on the properties of polycrystalline zirconia containing metastable tetragonal phase. J Mater Sci 1978;13:1464–70. https://doi.org/10.1007/BF00553200.

[14] Kosmač T, Oblak Č, Marion L. The effects of dental grinding and sandblasting on ageing and fatigue behavior of dental zirconia (Y-TZP) ceramics. J Eur Ceram Soc 2008;28:1085–90. https://doi.org/10.1016/j.jeurceramsoc.2007.09.013.

[15] Grigore A, Spallek S, Petschelt A, Butz B, Spiecker E, Lohbauer U. Microstructure of veneered zirconia after surface treatments: a TEM study. Dent Mater 2013;29:1098–107. https://doi.org/10.1016/j.dental.2013.07.022.

[16] Smielak B, Klimek L. Effect of hydrofluoric acid concentration and etching duration on select surface roughness parameters for zirconia. J Prosthet Dent 2015;113:596–602. https://doi.org/10.1016/j.prosdent.2015.01.001.

[17] Ackerl N, Wegener K. Ablation characteristics of alumina and zirconia ceramics on ultra-short pulsed laser machining. J Laser Micro Nanoeng 2019;14:168–72. https://doi.org/10.2961/jlmn.2019.02.0009.

[18] Delgado-Ruíz RA, Calvo-Guirado JL, Moreno P, Guardia J, Gomez-Moreno G, Mate-Sánchez JE, et al. Femtosecond laser microstructuring of zirconia dental implants. J Biomed Mater Res Part B Appl Biomater 2011;96B:91–100. https://doi.org/10.1002/jbm.b.31743.

[19] Yamamuro Y, Shimoyama T, Yan J. Microscale surface patterning of zirconia by femtosecond pulsed laser irradiation. Int J Precis Eng Manuf Technol 2022;9:619–32. https://doi.org/10.1007/s40684-021-00362-3.

[20] Feng D, Shen H. Hole quality control in underwater drilling of yttria-stabilized zirconia using a picosecond laser. Opt Laser Technol 2019;113:141–9. https://doi.org/10.1016/j.optlastec.2018.12.019.

[21] Cai Y, Chang W, Luo X, Qin Y. Superhydrophobicity of microstructured surfaces on zirconia by nanosecond pulsed laser. J Micromanufacturing 2019;2:5–14. https://doi.org/10.1177/2516598418799933.

[22] Roitero E, Lasserre F, Roa JJ, Anglada M, Mücklich F, Jiménez-Piqué E. Nanosecond-laser patterning of 3Y-TZP: damage and microstructural changes. J Eur Ceram Soc 2017;37:4876–87. https://doi.org/10.1016/j.jeurceramsoc.2017.05.052.

[23] Taylor LL, Qiao J, Qiao J. Optimization of femtosecond laser processing of silicon via numerical modeling. Opt Mater Express 2016;6:2745. https://doi.org/10.1364/ome.6.002745.

[24] Wang L, Wang X, Wang X, Liu Q. Laser drilling sub-10 nm holes on an island-shaped indium thin film. Appl Surf Sci 2020;527:146771. https://doi.org/10.1016/j.apsusc.2020.146771.

[25] Boulouz M, Martin L, Boulouz A, Boyer A. Effect of the dopant content on the physical properties of Y2O3-ZrO2 and CaO-ZrO2 thin films produced by evaporation and sputtering techniques. Mater Sci Eng B 1999;67:122–31. https://doi.org/10.1016/S0921-5107(99)00338-4.

[26] Parry JP, Shephard JD, Hand DP, Moorhouse C, Jones N, Weston N. Laser micromachining of zirconia (Y-TZP) ceramics in the picosecond regime and the impact on material strength. Int J Appl Ceram Technol 2011;8:163–71. https://doi.org/10.1111/j.1744-7402.2009.02420.x.

[27] Muñoz Tabares JA, Anglada MJ. Quantitative analysis of monoclinic phase in 3Y-TZP by Raman spectroscopy. J Am Ceram Soc 2010;93:1790. https://doi.org/10.1111/j.1551-2916.2010.03635.x. −5.

[28] Jeong S, Lee JY, Lee SS, Oh SW, Lee HH, Seo YH, et al. Chemically improved high performance printed indium gallium zinc oxide thin-film transistors. J Mater Chem 2011;21:17066–70. https://doi.org/10.1039/c1jm13767k.

[29] Liu GX, Liu A, Meng Y, Shan FK, Shin BC, Lee WJ, et al. Annealing dependence of solution-processed ultra-thin ZrOx films for gate dielectric applications. J Nanosci Nanotechnol 2015;15:2185–91. https://doi.org/10.1166/jnn.2015.10228.

[30] Matsui K. Phase-transformation mechanism in yttria-stabilized tetragonal zirconia polycrystal: discovery of grain boundary segregation-induced phase transformation. TOSOH Res Technol Rev 2010;54:3–15.

[31] Bayati R, Molaei R, Richmond A, Nori S, Wu F, Kumar D, et al. Modification of properties of yttria stabilized zirconia epitaxial thin films by excimer laser annealing. ACS Appl

Mater Interfaces 2014;6:22316–25. https://doi.org/10.1021/am506298y.

[32] Harai T, Hirota M, Hayakawa T, Shimada K, Mizutani M, Kuriyagawa T. Imparting biocompatibility to zirconia implants with nanosecond pulsed laser : formation of microgrooves and investigation of heat effects. J JAPAN Inst Met Mater 2019;83:37–45. https://doi.org/10.2320/jinstmet.J2018043.

[33] Heiroth S, Koch J, Lippert T, Wokaun A, Günther D, Garrelie F, et al. Laser ablation characteristics of yttria-doped zirconia in the nanosecond and femtosecond regimes. J Appl Phys 2010;107. https://doi.org/10.1063/1.3275868.

[34] Wenzel RN. Resistance of solid surfaces to wetting by water. Ind Eng Chem 1936;28:988–94. https://doi.org/10.1021/ie50320a024.

[35] Cassie ABD, Baxter S. Wettability of porous surfaces. Trans Faraday Soc 1944;40:546–51. https://doi.org/10.1039/tf9444000546.

[36] Zhang Y, Zou G, Liu L, Zhao Y, Liang Q, Wu A, et al. Time-dependent wettability of nano-patterned surfaces fabricated by femtosecond laser with high efficiency. Appl Surf Sci 2016;389:554–9. https://doi.org/10.1016/j.apsusc.2016.07.089.